


Local hybrid Allen-Cahn model in phase-field lattice Boltzmann method for incompressible two-phase flow

Dong Hun Kang  and Tae Sup Yun **School of Civil and Environmental Engineering, Yonsei University, Seoul 03722, Korea* (Received 13 December 2021; revised 6 March 2022; accepted 19 March 2022; published 11 April 2022)

For simulating incompressible two-phase fluid flows, several phase-field lattice Boltzmann (LB) methods based on the local Allen-Cahn (AC) equation have been intensively proposed in recent years. We present a local hybrid AC model for the phase-field LB method. In the proposed model, the local and nonlocal AC equations are linearly combined using a local weight assigned in the interface or bulk phase regions individually. Five numerical problems, namely diagonal translation, Zalesak's disk rotation, static bubble, two bubbles of different radii, and Rayleigh-Taylor instability, are simulated for validation. The numerical results agree well with the analytical solutions or available previous results. Additionally, the numerical dispersion and the coarsening phenomenon are considerably suppressed in the proposed model. Finally, the performance of the proposed model is validated by conducting a drainage simulation in porous media and compared with the global hybrid AC model.

DOI: [10.1103/PhysRevE.105.045307](https://doi.org/10.1103/PhysRevE.105.045307)

I. INTRODUCTION

Incompressible two-phase fluid flows are significant in nature and engineering applications, such as unsaturated soils, hydrocarbon production, microfluidic devices, and geological carbon storage. Implementation of numerical models for simulating two-phase flows often involves challenges such as complex interface dynamics, high contrasts in density and viscosity, and high surface tension. A lattice Boltzmann (LB) method was originally developed from lattice gas cellular automata for solving a Navier-Stokes equation describing fluid flow [1–4]. It is being extended to generalized numerical solvers for partial differential equations such as a Poisson equation, a convection-diffusion equation [4–7]. The LB method for two-phase flows has been intensively investigated and discussed in the last two decades [3,8–11]. Two-phase flow models based on the LB method include the color-gradient [12–15], pseudopotential [12,16,17], free-energy [12,18], and phase-field models [19–22]. The color-gradient and pseudopotential models are advantageous for simulating two-phase flows in porous media, owing to their simplicity and rigorous volume and mass conservation properties [14–16,23]. However, they often suffer from high spurious velocity and small ranges of numerical conditions available. Among phase-field LB methods, the Cahn-Hilliard (CH) method has attracted attention for incompressible two-phase flows because it can accurately express complex interface dynamics [19,20]. However, from a theoretical viewpoint, the fourth-order CH equation cannot be directly recovered via the second-order Chapman-Enskog expansion [24]. A bubble shrinkage (i.e., mass loss of secondary phase) can occur when a bubble radius becomes smaller than a critical value depending on the domain size [25]. Recently, the Allen-Cahn (AC)

model has been explored for incompressible two-phase flows. The classical AC model for phenomenologically describing a phase transition is nonconservative in mass and involves a second-order spatial derivative. For the mass conservative property, two classes of the AC model are developed. One is the nonlocal AC (NAC) model in which a Lagrange multiplier was adopted to preserve global mass conservation [26]. The other is the local AC (LAC) model, developed by Sun and Beckermann [27] and later reformulated by Chiu and Lin [28], which ensures mass conservation without any Lagrange multiplier. A phase-field LB method based on the LAC model was first developed with a single relaxation time in Geier *et al.* [22]. Thereafter, other studies have proposed several LAC-type phase-field LB methods [21,24], which, however, suffered from numerical dispersion, resulting in high-order parameter fluctuation in a bulk phase region [21,29]. To resolve the numerical dispersion, Hu *et al.* [29] proposed the global hybrid AC (GHAC) model by a linear combination of LAC and NAC equations using a single global weight. The GHAC model reduced the numerical dispersion better as compared with LAC models. However, the NAC model inherently involves the coarsening process, in which mass of smaller bubbles is gradually transferred to bigger bubbles and eventually smaller bubbles disappear [30,31]. Additionally, the GHAC model partially inherits the coarsening process from the NAC model. Although coarsening is a basic physical phenomenon observed in nature (e.g., oil-in-water emulsion polymerization), it is less important for two-phase fluid systems dominated by hydrodynamic flow. Furthermore, in the NAC and GHAC models, the rate of the coarsening process cannot be independently controlled. Thus, one must suppress the coarsening phenomenon in the GHAC model for a more consistent and accurate two-phase flow simulation.

In this study, we propose a local hybrid AC (LHAC) model for the phase-field LB method; the framework of the model is established using the original GHAC model in Hu *et al.* [29],

*taesup@yonsei.ac.kr

LB equation for the LAC model in Liang *et al.* [24], and LB equation for incompressible flows in Liang *et al.* [20]. The LB equations used in this study are not newly derived; however, the proposed LHAC model and an estimation method of phase interface region were able to reduce the drawbacks in the LAC and NAC models while preserving their advantages. The proposed model is validated with five standard benchmarks and compared with the LAC and GHAC models. A simulation of drainage process in 2D porous media further corroborates the stability of the proposed model.

II. MATHEMATICAL MODELS AND NUMERICAL METHODS

A. LHAC model

The governing equations of incompressible two-phase flows with the hybrid-type AC model can be expressed as follows [29]:

$$\nabla \cdot \mathbf{u} = 0, \quad (1)$$

$$\frac{\partial \rho \mathbf{u}}{\partial t} + \nabla \cdot (\rho \mathbf{u} \mathbf{u}) = -\nabla p + \nabla \cdot (\mu(\nabla \mathbf{u} + \nabla \mathbf{u}^T)) + \mathbf{F}, \quad (2)$$

$$\frac{\partial \phi}{\partial t} + \nabla \cdot (\phi \mathbf{u}) = M_\phi \nabla^2 \phi + D_L + D_{NL}, \quad (3)$$

where \mathbf{u} represents local velocity, ρ density, p pressure, μ dynamic viscosity, \mathbf{F} body force (including a surface tension force), and M_ϕ mobility. An order parameter ϕ represents a given fluid R (red) and B (blue) as 0.5 and -0.5 , respectively. D_L and D_{NL} denote source terms for preserving a phase interface by the LAC and NAC models, respectively.

In a plane interface, a one-dimensional profile of ϕ along a z direction in an equilibrium state is defined as [22,32]

$$\phi^{eq}(z) = \frac{1}{2} \tanh\left(\frac{2}{W}z\right), \quad (4)$$

where W represents a positive constant controlling the interface thickness.

The local density and kinematic viscosity of a binary mixture are obtained by interpolating each property using ϕ as follows [33]:

$$\rho = \left(\frac{1}{2} + \phi\right)\rho_R + \left(\frac{1}{2} - \phi\right)\rho_B, \quad (5)$$

$$\frac{1}{\nu} = \frac{\frac{1}{2} + \phi}{\nu_R} + \frac{\frac{1}{2} - \phi}{\nu_B}, \quad (6)$$

where ρ_k and ν_k represent the bulk density and kinematic viscosity of fluid k (R or B), respectively.

The source terms D_L and D_{NL} in the GHAC model are given as follows [29]:

$$D_L = -\lambda M_\phi \nabla \cdot \left(\frac{4}{W}\left(\frac{1}{2} + \phi\right)\left(\frac{1}{2} - \phi\right)\mathbf{n}\right), \quad (7)$$

$$D_{NL} = (1 - \lambda)M_\phi \frac{32\phi\left(\frac{1}{2} + \phi\right)\left(\frac{1}{2} - \phi\right)}{W^2} + \gamma(t)\left(\frac{1}{2} + \phi\right)\left(\frac{1}{2} - \phi\right), \quad (8)$$

where λ and $(1-\lambda)$ represent global weights for the LAC and NAC source terms, respectively. An interface unit normal vector \mathbf{n} is given by $\nabla\phi/|\nabla\phi|$. The Lagrange multiplier $\gamma(t)$ for enforcing a global mass conservation over a domain Ω at time t can be obtained as follows [26,31]:

$$\gamma(t) = -\frac{\int_\Omega (1 - \lambda)M_\phi \frac{32\phi\left(\frac{1}{2} + \phi\right)\left(\frac{1}{2} - \phi\right)}{W^2} dV}{\int_\Omega \left(\frac{1}{2} + \phi\right)\left(\frac{1}{2} - \phi\right) dV}. \quad (9)$$

Applying the Lagrange multiplier can preserve the global mass. However, the coarsening phenomenon still occurs in both the NAC and GHAC models owing to a violation in the conservation of local mass. The violation in an entire domain is relatively much higher in an interface region than in a bulk phase region (see Appendix, Sec. 1). Here, the interface region conceptually means a region of finite thickness in which the spatial transition of two fluids exists in the phase-field model. To suppress the coarsening process in the LHAC model, a simulation domain Ω was partitioned into an interface region Ω_I and a bulk phase region Ω_B , where the LAC and GHAC models were separately applied. Therefore, the global weight λ in Eqs. (7)–(9) was replaced by a local weight $\Lambda(\mathbf{x})$, which was conditionally defined for Ω_I and Ω_B as follows:

$$\Lambda(\mathbf{x}) = \begin{cases} 1 & \mathbf{x} \in \Omega_I \\ \lambda_B & \mathbf{x} \in \Omega_B \end{cases}, \quad (10)$$

with

$$\Omega = \Omega_I \cup \Omega_B \text{ and } \emptyset = \Omega_I \cap \Omega_B,$$

where λ_B is a weight constant of the LAC and NAC models in Ω_B .

By using the local weight Λ from Eq. (10), the phase-field equation in Ω_I is governed by the LAC model, while Ω_B is still subjected to the GHAC model. Noteworthy, the Lagrange multiplier term in Eq. (8) still globally applies over Ω . This approach can achieve not only accurate interface dynamics in Ω_I but also the suppression of both the numerical dispersion in Ω_B and the coarsening phenomenon. The estimation of Ω_I is presented in the next section and the detailed performances of the proposed model are also discussed in Sec. III.

B. Interface region estimation

To implement Eq. (10), it is a prerequisite that the interface region Ω_I is relevantly estimated from an order parameter field, which may have been contaminated by the numerical dispersion. Let us consider an estimator of Ω_I in a 1D space for the sake of simplicity. Suppose a 1D profile of an actual order parameter ϕ^{ac} , perpendicularly crossing an exact interface, comprises an equilibrium component ϕ^{eq} and a small perturbation component $\delta\phi$:

$$\phi^{ac}(z) = \phi^{eq}(z) + \delta\phi(z). \quad (11)$$

The inverse function of Eq. (11) yields

$$\frac{z}{W} = \frac{1}{2} \tanh^{-1}(2\phi^{eq}) = \frac{1}{2} \tanh^{-1}(2(\phi^{ac}(z) - \delta\phi(z))), \quad (12)$$

where z is the inverse hyperbolic tangent function of ϕ^{eq} and tends to be insensitive to the small perturbation $\delta\phi$ unless ϕ^{ac} approaches ± 0.5 . A line of $z = 0$ can be defined as the exact interface line.

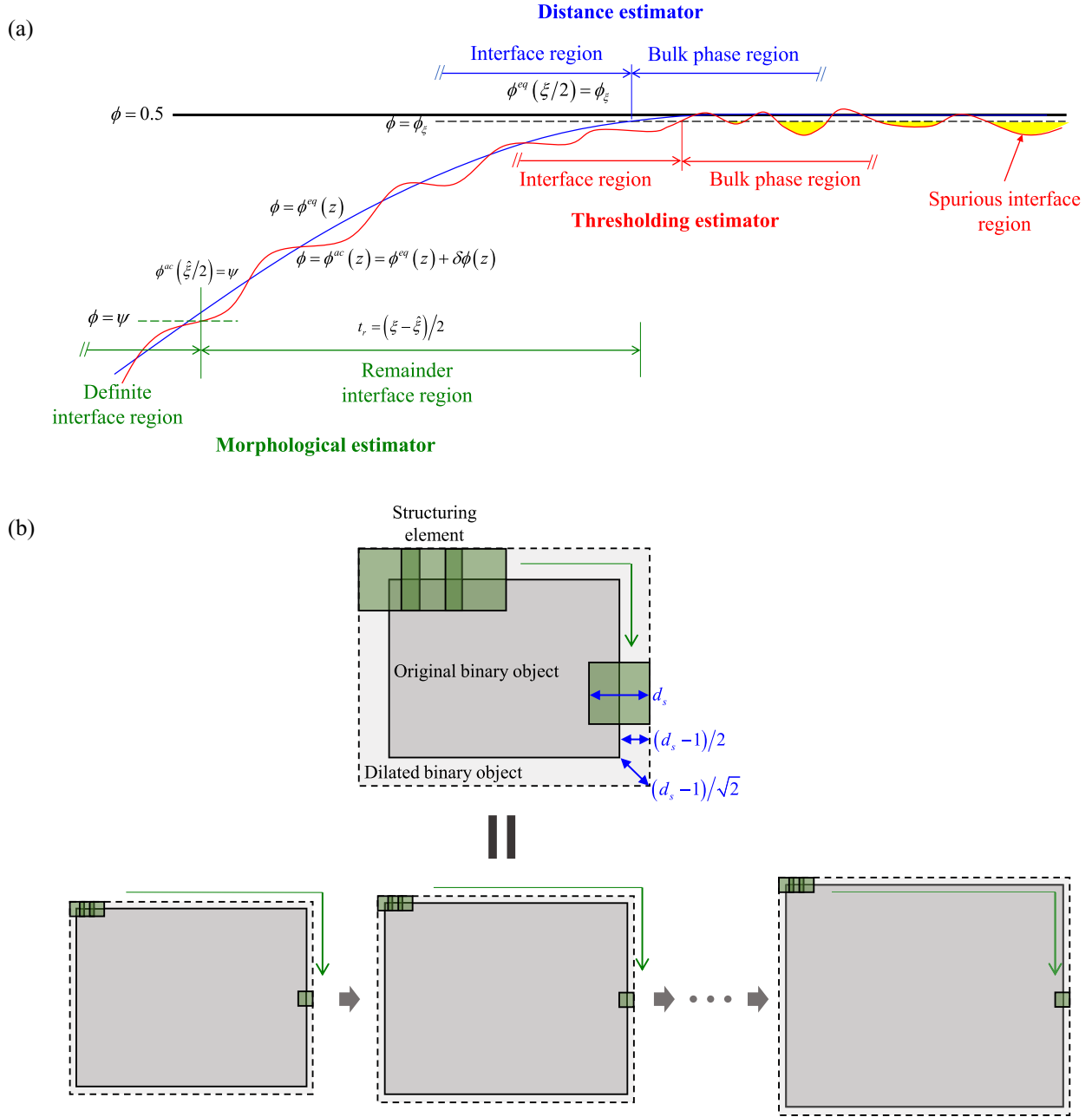


FIG. 1. Schematics of (a) three different estimators for determining interface region in order parameter profile and (b) morphological dilation by square-shaped structuring element in 2D space.

A thresholding-based estimator segments the interface region Ω_I from a field of ϕ^{ac} using a single-threshold value ϕ_ξ with the thresholding method as

$$\Omega_I = \{x | |\phi^{ac}(x)| \leq \phi_\xi\}, \quad (13)$$

where a single-threshold value ϕ_ξ is an order parameter value with respect to an interface boundary as $|\phi^{eq}(\pm\xi/2)| = \phi_\xi$, where ξ is an interface thickness and we let $\Delta_\xi = 0.5 - \phi_\xi$. Note that Δ_ξ must be a sufficiently small positive value to suppress the coarsening effect.

Because z exponentially approaches positive or negative infinity as ϕ^{eq} approaches $\pm 1/2$, $\delta\phi$ hinders directly segmenting Ω_I by the thresholding estimator. If we use the thresholding estimator for Ω_I , spurious interface regions, in which

$|\phi^{ac}| \leq \phi_\xi \leq |\phi^{eq}|$, will be additionally segmented from the bulk phase region as shown in Fig. 1(a). Another intuitive estimator for Ω_I is a distance from a nearest exact interface line and can determine Ω_I as

$$\Omega_I = \{x | |x - x(\phi^{eq} = 0)| \leq \frac{1}{2}\xi\}. \quad (14)$$

However, it is very difficult and expensive to directly estimate a distance from all possible pixels to the nearest exact interface line from an order parameter field defined in a Cartesian grid space. Instead, this study proposes an alternative estimator for Ω_I that uses both the threshold- and distance-based criteria with a morphological operation. As mentioned above, the effect of $\delta\phi$ in Eq (12) can be negligible when $|\phi^{ac}|$ is moderately smaller than $1/2$. This implies that we can

accurately segment only a part of Ω_I by a relevant threshold value ψ as

$$\hat{\Omega}_I = \{x | |\phi^{ac}(x)| \leq \psi\} \text{ and } \hat{\Omega}_I \subset \Omega_I \text{ for } \phi_\xi - \psi \gg \sup |\delta\phi|, \quad (15)$$

where $\hat{\Omega}_I$ is herein called a definite interface region. A thickness of $\hat{\Omega}_I$ is presented by Eq. (12) as

$$\hat{\xi} = W \tanh^{-1}(2(\psi - \delta\phi)) \approx W \tanh^{-1}(2\psi). \quad (16)$$

A remainder interface region $\hat{\Omega}_I^C$ which is a complementary region of $\hat{\Omega}_I$ in Ω_I is then defined as

$$\hat{\Omega}_I^C = \{x | \exists x : |x - y| \leq t_r, y \in \hat{\Omega}_I, x \in (\Omega - \hat{\Omega}_I)\}, \quad (17)$$

where the geometry of $\hat{\Omega}_I^C$ will be almost a form wrapping $\hat{\Omega}_I$ by two sides. A one-side thickness of $\hat{\Omega}_I^C$ is given by $t_r = (\xi - \hat{\xi})/2$.

In the 2D or 3D Cartesian space, Eq. (17) is easier and more efficient than Eq. (14) because a Euclidean distance transform used in digital image processing is available. Nonetheless, this is also an expensive operation to iterate over every time step.

A morphological dilation can be an efficient way to approximately determine $\hat{\Omega}_I^C$. In the digital image processing, a morphological dilation for a binary object \mathbf{A} by a structuring element \mathbf{B} in an integer Cartesian space Ω^i is defined as [see Fig. 1(b)]

$$\mathbf{A} \oplus \mathbf{B} = \{\mathbf{x} | (\mathbf{x} - \mathbf{y} + \mathbf{y}_c) \in \mathbf{A}, \mathbf{x} \in \Omega^i, \mathbf{y} \in \mathbf{B}, \mathbf{y}_c = \text{center}(\mathbf{B}) \text{ and } \mathbf{y}_c \in \mathbf{B}\}, \quad (18)$$

where \mathbf{x} and \mathbf{y} are integer coordinate of pixels. \oplus is the morphological dilation operator. A length of grid spacing in Ω^i is unity.

If a square (or cube)-shaped binary object $\mathbf{s}(d_s)$ with a side length d_s is used as a structuring element, the dilation of \mathbf{A} by $\mathbf{s}(d_s)$ can be replaced by a process in which \mathbf{A} is sequentially dilated $(d_s - 1)/2$ times by the smallest structuring elements $\mathbf{s}(3)$ as

$$\mathbf{A} \oplus \mathbf{s}(d_s) = \underbrace{((\mathbf{A} \oplus \mathbf{s}(3)) \oplus \dots \oplus \mathbf{s}(3))}_{(d_s-1)/2}, \quad (19)$$

where d_s is set to an odd positive number to meet the operation symmetry. The thickness dilated by $\mathbf{s}(d_s)$ is between $(d_s - 1)/2$ and $(d_s - 1)\sqrt{d}/2$; here, d is dimension.

Because the morphological dilation of \mathbf{A} by $\mathbf{s}(3)$ can be simply implemented by searching in every candidate pixel whether a neighboring pixel belongs to \mathbf{A} , no calculation of distance is required. The dilated pixels by Eq. (19) are analogous to the estimated region by Eq. (17).

In the LB method, the domain is usually defined as an integer Cartesian space, combining Eqs. (15), (17), (18), and (19); the morphological dilation-based estimator for Ω_I is presented as

$$\Omega_I = \hat{\Omega}_I \oplus \mathbf{s}(d_s) = \hat{\Omega}_I \oplus \underbrace{\mathbf{s}(3) \oplus \dots \oplus \mathbf{s}(3)}_{(d_s-1)/2} \text{ and} \\ \hat{\Omega}_I = \{\mathbf{x} | |\phi(\mathbf{x})| \leq \psi, \mathbf{x} \in \Omega\}. \quad (20)$$

In Eq. (20), the dilated thickness must be greater than or equal to the one-side thickness t_r as $(d_s - 1)/2 \geq t_r$ and so d_s

is expressed as an inequality:

$$d_s \geq W \tanh^{-1}(2\phi_\xi) - W \tanh^{-1}(2\psi) + 1. \quad (21)$$

Further, we select d_s of a minimum odd positive number by a ceiling function as

$$d_s = 2 \left\lceil \frac{W}{2} (\tanh^{-1}(2\phi_\xi) - \tanh^{-1}(2\psi)) \right\rceil + 1. \quad (22)$$

This study used the morphological dilation-based estimator to determine Ω_I in the simulations.

C. LB model for phase-field equation

The multirelaxation time (MRT)-LB model was used to solve the AC model in this study. The LB equation comprises streaming and collision equations as follows [20,24]:

$$g_i(\mathbf{x} + \mathbf{e}_i \delta t, t + \delta t) = \tilde{g}_i(\mathbf{x}, t), \quad (23)$$

$$\tilde{\mathbf{g}}(\mathbf{x}, t) = \mathbf{g}(\mathbf{x}, t) - \mathbf{M}^{-1} \mathbf{S}_g \mathbf{M} (\mathbf{g} - \mathbf{g}^{eq}) \\ + \mathbf{M}^{-1} (\mathbf{I} - \frac{1}{2} \mathbf{S}_g) \mathbf{M} \mathbf{G}_g, \quad (24)$$

where g_i is a particle distribution function with a discrete particle velocity \mathbf{e}_i at position \mathbf{x} and time t . $\tilde{\mathbf{g}} = [\tilde{g}_0, \tilde{g}_1, \dots, \tilde{g}_{q-1}]^T$, $\mathbf{g} = [g_0, g_1, \dots, g_{q-1}]^T$, and $\mathbf{g}^{eq} = [g_0^{eq}, g_1^{eq}, \dots, g_{q-1}^{eq}]^T$ are column vectors of the postcollision, precollision, and equilibrium distribution functions in a $DdQq$ lattice model, respectively. \mathbf{M} denotes a transformation matrix, \mathbf{S}_g a diagonal relaxation matrix, and $\mathbf{G}_g = [G_0^g, G_1^g, \dots, G_{q-1}^g]^T$ a source term.

The equilibrium distribution function is given as [24]

$$g_i^{eq} = w_i \phi \left(1 + \frac{\mathbf{e}_i \cdot \mathbf{u}}{c_s^2} \right), \quad (25)$$

where w_i represents the directional weight, and c_s the speed of sound in the lattice system.

The source term G_i^g with antidiffusion terms of Eqs. (7) and (8) is defined as follows [24,29]:

$$G_i^g = w_i \left(\frac{1}{c_s^2} \mathbf{e}_i \cdot \mathbf{Q}^L + Q^{NL} \right), \quad (26)$$

where \mathbf{Q}^L is given as follows:

$$\mathbf{Q}^L = c_s^2 \Lambda \frac{4(\frac{1}{2} + \phi)(\frac{1}{2} - \phi)}{W} \mathbf{n} + \partial_t(\phi \mathbf{u}). \quad (27)$$

The time derivative term $\partial_t(\phi \mathbf{u})$ eliminates the artificial term in the recovered AC equation [6,24]. To avoid the implicitness of ϕ in Eq. (9), Q^{NL} is given by replacing ϕ with $\hat{\phi}$ as follows:

$$Q^{NL} = (1 - \Lambda) M_\phi \frac{32\phi(\frac{1}{2} + \hat{\phi})(\frac{1}{2} - \hat{\phi})}{W^2} \\ + \gamma(t) (\frac{1}{2} + \hat{\phi})(\frac{1}{2} - \hat{\phi}). \quad (28)$$

Additionally, $\hat{\phi}$ is used to determine Ω_I and Ω_B in Eq. (20), so that Λ can be evaluated at the current time step. Similarly, Eq. (9) is modified to calculate the Lagrange multiplier γ as

follows:

$$\gamma(t) = -\frac{32M_\phi}{W^2} \frac{\sum_{\mathbf{x} \in \Omega} (1 - \Lambda) \hat{\phi} \left(\frac{1}{2} + \hat{\phi}\right) \left(\frac{1}{2} - \hat{\phi}\right)}{\sum_{\mathbf{x} \in \Omega} \left(\frac{1}{2} + \hat{\phi}\right) \left(\frac{1}{2} - \hat{\phi}\right)}. \quad (29)$$

The order parameter ϕ is calculated by the zeroth-order moment of g_i with the source term Q^{NL} as follows [29]:

$$\phi = \hat{\phi} + \frac{\delta t}{2} Q^{NL} = \sum_i g_i + \frac{\delta t}{2} Q^{NL}. \quad (30)$$

The discrete velocity set and the corresponding directional weights in the D2Q9 lattice model are defined as follows:

$$\mathbf{e}_i = \begin{cases} (0, 0)c \\ (\pm 1, 0)c, (0, \pm 1)c \\ (\pm 1, \pm 1)c, (\pm 1, \mp 1)c \end{cases} \quad \text{and} \quad (31)$$

$$w_i = \begin{cases} 4/9 & i = 0 \\ 1/9 & \text{for } i = 1 - 4, \\ 1/36 & i = 5 - 8 \end{cases}$$

where the lattice velocity c is $\delta x / \delta t$. The speed of sound c_s is $c / \sqrt{3}$ in the D2Q9 lattice model. δx and δt are usually set to unity.

In the MRT model, the transformation matrix \mathbf{M} for mapping the distribution functions from the discrete velocity space to the moment space is defined as follows [34,35]:

$$\mathbf{M} = \begin{bmatrix} 1 & 1 & 1 & 1 & 1 & 1 & 1 & 1 & 1 \\ -4 & -1 & -1 & -1 & -1 & 2 & 2 & 2 & 2 \\ 4 & -2 & -2 & -2 & -2 & 1 & 1 & 1 & 1 \\ 0 & 1 & -1 & 0 & 0 & 1 & -1 & 1 & -1 \\ 0 & -2 & 2 & 0 & 0 & 1 & -1 & 1 & -1 \\ 0 & 0 & 0 & 1 & -1 & 1 & -1 & -1 & 1 \\ 0 & 0 & 0 & -2 & 2 & 1 & -1 & -1 & 1 \\ 0 & 1 & 1 & -1 & -1 & 0 & 0 & 0 & 0 \\ 0 & 0 & 0 & 0 & 0 & 1 & 1 & -1 & -1 \end{bmatrix}. \quad (32)$$

The moments of the equilibrium distribution functions and the source terms are then presented as follows:

$$\mathbf{M} \mathbf{g}^{eq} = \begin{bmatrix} \phi \\ -2\phi \\ \phi \\ \phi u_x \\ -\phi u_x \\ \phi u_y \\ -\phi u_y \\ 0 \\ 0 \end{bmatrix} \quad \text{and} \quad \mathbf{M} \mathbf{G}^s = \begin{bmatrix} Q^{NL} \\ -2Q^{NL} \\ Q^{NL} \\ Q_x^L \\ -Q_x^L \\ Q_y^L \\ -Q_y^L \\ 0 \\ 0 \end{bmatrix}. \quad (33)$$

The diagonal relaxation matrix \mathbf{S}_g in this study is chosen as follows [29]:

$$\mathbf{S}_g = \text{diag}(1, 1.1, 1.1, 1/\tau_g, 1/\tau_g, 1/\tau_g, 1/\tau_g, 1.2, 1.2), \quad (34)$$

where the relaxation time τ_g is a function of mobility as follows:

$$\tau_g = \frac{M_\phi}{c_s^2} + \frac{1}{2}. \quad (35)$$

Noteworthy, the relaxation times in Eq. (34) yield the stable and accurate performances.

In this study, the time derivative $\partial_t(\phi \mathbf{u})$ and the order-parameter gradient $\nabla \phi$ are calculated by the backward difference and the isotropic central difference schemes as follows [33]:

$$\partial_t(\phi \mathbf{u}) = \frac{(\phi \mathbf{u})|_t - (\phi \mathbf{u})|_{t-\delta t}}{\delta t} \quad (36)$$

$$\nabla \phi(\mathbf{x}) = \sum_i \frac{w_i \mathbf{e}_i \phi(\mathbf{x} + \mathbf{e}_i \delta t)}{c_s^2 \delta t}. \quad (37)$$

D. LB model for incompressible flows

The MRT-LB model for the hydrodynamic equation in incompressible flows can be expressed as follows [20]:

$$f_i(\mathbf{x} + \mathbf{e}_i \delta t, t + \delta t) = \tilde{f}_i(\mathbf{x}, t), \quad (38)$$

$$\tilde{\mathbf{f}}(\mathbf{x}, t) = \mathbf{f}(\mathbf{x}, t) - \mathbf{M}^{-1} \mathbf{S} \mathbf{M} (\mathbf{f} - \mathbf{f}^{eq}) + \mathbf{M}^{-1} (\mathbf{I} - \frac{1}{2} \mathbf{S}) \mathbf{M} \mathbf{G}, \quad (39)$$

where f_i is a particle distribution function with the discrete particle velocity \mathbf{e}_i at position \mathbf{x} and time t . $\tilde{\mathbf{f}} = [\tilde{f}_0, \tilde{f}_1, \dots, \tilde{f}_{q-1}]^T$, $\mathbf{f} = [f_0, f_1, \dots, f_{q-1}]^T$, and $\mathbf{f}^{eq} = [f_0^{eq}, f_1^{eq}, \dots, f_{q-1}^{eq}]^T$ also represent column vectors of the postcollision, precollision, and equilibrium distribution functions. \mathbf{S} denotes a diagonal relaxation matrix, $\mathbf{G} = [G_0, G_1, \dots, G_{q-1}]^T$ a forcing term.

The equilibrium distribution function f_i^{eq} is chosen as follows [20,24]:

$$f_i^{eq} = \frac{p}{c_s^2} (w_i - \delta_{0i}) + \rho s_i(\mathbf{u}), \quad (40)$$

where δ_{0i} is Kronecker delta, and s_i is defined as follows:

$$s_i(\mathbf{u}) = w_i \left(\frac{\mathbf{e}_i \cdot \mathbf{u}}{c_s^2} + \frac{(\mathbf{e}_i \cdot \mathbf{u})^2}{2c_s^4} - \frac{\mathbf{u} \cdot \mathbf{u}}{2c_s^2} \right). \quad (41)$$

The forcing term G_i considering the density difference is given by [24,36]

$$G_i = w_i \left(\frac{\mathbf{e}_i \cdot \mathbf{F} - \mathbf{u} \cdot \mathbf{F}}{c_s^2} + \frac{(\mathbf{e}_i \cdot \mathbf{u}) \mathbf{e}_i}{c_s^4} \cdot (\mathbf{F} + c_s^2 \nabla \rho) \right), \quad (42)$$

where the density gradient is $\nabla \rho = (\rho_R - \rho_B) \nabla \phi$.

Thereafter, the equilibrium distribution functions and forcing terms are expressed in the moment space as follows:

$$\mathbf{M} \mathbf{f}^{eq} = \begin{bmatrix} 0 \\ 6p + 3\rho \mathbf{u} \cdot \mathbf{u} \\ -(9p + 3\rho \mathbf{u} \cdot \mathbf{u}) \\ \rho u_x \\ -\rho u_x \\ \rho u_y \\ -\rho u_y \\ \rho(u_x^2 - u_y^2) \\ \rho u_x u_y \end{bmatrix} \quad \text{and}$$

$$\mathbf{MG} = \begin{bmatrix} \mathbf{u} \cdot \nabla \rho \\ 6\mathbf{u} \cdot \mathbf{F} \\ -6\mathbf{u} \cdot \mathbf{F} - \mathbf{u} \cdot \nabla \rho \\ F_x \\ -F_x \\ F_y \\ -F_y \\ 2(u_x F_x - u_y F_y) + 2c_s^2(u_x \partial_x \rho - u_y \partial_y \rho) \\ u_x F_y + u_y F_x + c_s^2(u_x \partial_y \rho + u_y \partial_x \rho) \end{bmatrix}. \quad (43)$$

The diagonal relaxation matrix \mathbf{S} in the hydrodynamic model is herein chosen as follows [37]:

$$\mathbf{S} = \text{diag}(1, 1, 1, 1, 1.7, 1, 1.7, 1/\tau, 1/\tau), \quad (44)$$

where the relaxation time τ is directly related to the kinematic viscosity ν as follows:

$$\tau = \frac{\nu}{c_s^2} + \frac{1}{2}. \quad (45)$$

After the streaming step, the macroscopic hydrodynamical quantities such as pressure and velocity are determined by the zeroth- and first-order moments of f_i as follows [20]:

$$p = \frac{c_s^2}{1 - w_0} \left(\sum_{i \neq 0} f_i + \frac{\delta t}{2} \mathbf{u} \cdot \nabla \rho + \rho s_0(\mathbf{u}) \right), \quad (46)$$

$$\rho \mathbf{u} = \sum_i f_i \mathbf{e}_i + \frac{\delta t}{2} \mathbf{F}. \quad (47)$$

The body force acting on the fluid comprises a surface tension force \mathbf{F}_s and other possible body force \mathbf{F}_b as follows:

$$\mathbf{F} = \mathbf{F}_s + \mathbf{F}_b. \quad (48)$$

The continuum surface force model is directly utilized for calculating \mathbf{F}_s as follows [38]:

$$\mathbf{F}_s = -\sigma \kappa \nabla \phi, \quad (49)$$

$$\kappa = \nabla_S \cdot \mathbf{n}, \quad (50)$$

where σ represents surface tension parameter. κ denotes a local curvature of the interface, and the surface differential operator is $\nabla_S = (\mathbf{I} - \mathbf{nn}) \cdot \nabla$.

III. MODEL VALIDATIONS

The proposed model was numerically validated via five standard benchmark tests: diagonal translation [22,29,39] and Zalesak's disk rotation [20,22] tests for evaluating the interface tracking under a predefined constant velocity field, and static bubble [24], two radii bubbles [31,40], and Rayleigh-Taylor instability (RTI) [20,41] tests for assessing the immiscible fluid flow. For the simulations, W and λ_B were set to 3 and 0.9, respectively, unless otherwise specified. Also, in this study, we chose $\psi = 0.495$ for determining $\hat{\Omega}_t$ and $\Delta_\xi = 0.5 - \phi_\xi = 10^{-5}$. The selection of these parameters is equivalent to a condition of $\xi = 17.27$ and the coarsening process can be practically suppressed (see Appendix, Sec. 1). Reportedly, the largest value $\delta\phi_{\max}$ of the fluctuation of the order parameter was up to $\sim 10^{-3}$ in previous bubble simulations by the LAC model [29] but those of this study could be

slightly different with them owing to the criterion of Ω_B . A squared domain was used with a periodic boundary condition for all boundaries, except for the RTI test. L_0 denotes a length of a domain.

A. Diagonal translation of circular interface

Interface tracking in the proposed model was validated by the diagonal translation of a circular interface under a constant velocity field $\mathbf{u} = (U_0, U_0)$. A circle of radius $R = L_0/5$ was initially placed at the center of the domain [see Fig. 2(a)]. To present the rate of error convergence according to grid size, as conducted in Ref. [39], six domains of different sizes were prepared with $L_0 = 100, 200, \dots, 600$. The constant velocity was $U_0 = 0.02$, and the time interval for the circle to return to the domain center depended upon the domain size of $T_0 = L_0/U_0$. The dimensionless Péclet number was set as $\text{Pe} = \frac{U_0 W}{M_\phi} = 60$ so that the mobility was $M_\phi = 0.001$. To measure the error of the proposed model in time-periodic problems, the L_2 norm error of the order parameter was defined as follows [39]:

$$E_\phi(t) = \sqrt{\frac{\sum_{\mathbf{x}} (\phi(\mathbf{x}, t) - \phi(\mathbf{x}, 0))^2}{\sum_{\mathbf{x}} (\phi(\mathbf{x}, 0))^2}}. \quad (51)$$

To focus on diagonal translation in the proposed model, the initial configuration of the order parameter $\phi(\mathbf{x}, 0)$ and the particle distribution functions $g_i(\mathbf{x}, 0)$ were prepared from another simulation under the zero-velocity field condition $\mathbf{u} = 0$ and iteration time T_0 . From Fig. 2(a), it is evident that the final circle with bluish solid line after ten cycles under $\mathbf{u} = (U_0, U_0)$ in the domain of $L_0 = 100$ coincided with the initial circle with red-colored dashed line. For the convergence study, the relative error $E_\phi(T_0)$ after one cycle was estimated for a domain with different size [see Fig. 2(b)]. The convergence rate was measured as 0.4 by linear regression, and it was slightly lower than the results in Geier *et al.* (2015) [22] and Hu *et al.* (2019) [29]. However, the magnitude of the relative errors in this study was overall smaller than those in the previous studies.

B. Zalesak's rotation

A circular disk with a slot was placed at the center of the domain and subjected to a vortex flow that rotated around the pinned center. The domain size L_0 was set as 200 with circle radius R of 80 and slot width l_s of 15. The time interval $T_0 = L_0/U_0$ was a duration of half rotation. U_0 and M_ϕ were set as 0.02 and 0.001 such that $\text{Pe} = 60$. The constant velocity field for the vortex flow was defined as follows:

$$u_x(x, y) = -U_0 \pi \left(\frac{y}{L_0} - \frac{1}{2} \right), \quad (52)$$

$$u_y(x, y) = U_0 \pi \left(\frac{x}{L_0} - \frac{1}{2} \right). \quad (53)$$

The initial configuration of the order parameter $\phi(\mathbf{x}, 0)$ was set by Eq. (4) using a signed distance from the initial disk interface. Figure 3 shows the interface levels ($\phi = 0$) of the rotated disk from the initial configuration ($t = 0$) to that after one cycle ($t = 2T_0$). Evidently, the interface of the

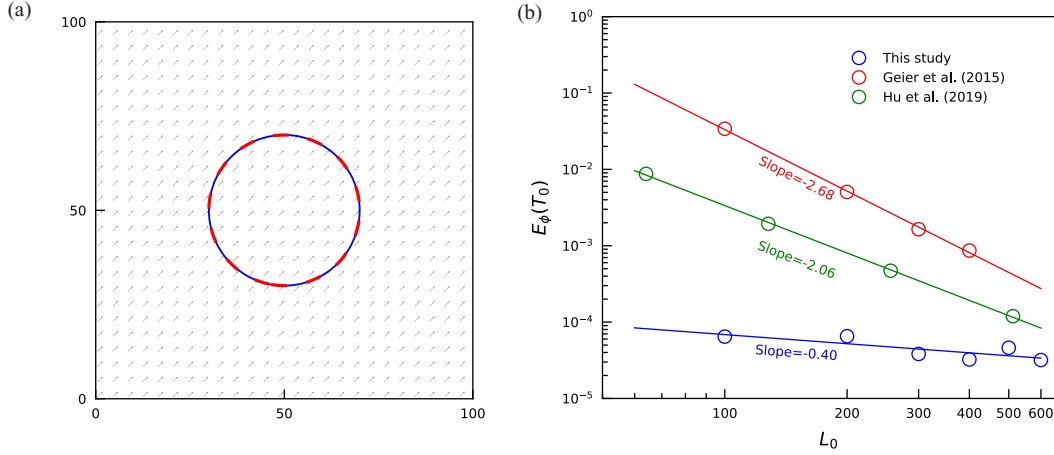


FIG. 2. Diagonal translation of a circular interface: (a) Moved (blue solid line) and initial (red dashed line) configurations after ten cycles. Gray arrows within a domain represent a constant velocity field $\mathbf{u} = (U_0, U_0)$. (b) Convergence rates of the L_2 norm error for different domain size L_0 at one cycle ($t = T_0$).

rotating disk maintained its initial geometry while the disk tip experienced an unnoticeable squash within acceptable level during the rotation. The disk returned to its original shape after one cycle.

C. Static bubble

A static bubble test was conducted to validate the magnitude of spurious velocity, the isotropy of bubble shape, and the development of pressure under the applied surface tension force. The relationship of bubble radius R with pressure difference Δp between the inside and outside of the bubble is given by the Young-Laplace equation in 2D as follows:

$$\Delta p = \frac{\sigma}{R}. \tag{54}$$

In this test, L_0 , M_ϕ , and σ were chosen as 201, 1/6, and 0.001, respectively. For the red and blue fluids, the density was set as $\rho_R = 1$ and $\rho_B = 0.001$, respectively. The relaxation time was $\tau = 0.8$ with respect to a kinematic viscosity of $\nu = 0.1$ for both fluids. The initial order parameter was assigned as follows:

$$\phi(\mathbf{x}, t = 0) = -\frac{1}{2} \tanh\left(\frac{2}{W}(|\mathbf{x} - \mathbf{x}_c| - R)\right), \tag{55}$$

where \mathbf{x}_c represents the domain center.

Six circles with different radii from $R = 10$ to 60 were initially placed at the domain center, and the iteration of each simulation continued for $t = 10^5$ sufficient to attain the steady

state. Figure 4(a) shows that the density profile (circular symbol) across the bubble center when R was 50 agreed well with the analytic solution (solid line) that was the initial density profile. The pressure profile in Fig. 4(b) was continuous near the interface, and no sharp fluctuation was observed. The isotropy in both the spurious velocity distribution and bubble interface shape was satisfied, as seen in Fig. 4(c), partially supporting that the surface tension force was well implemented. In Fig. 4(c), the magnitude of the maximum spurious velocity, $|\mathbf{u}_{\max}|$ was approximately 2.6×10^{-6} . Furthermore, the simulated pressure difference Δp for different bubble radii was consistent compared with the Young-Laplace equation, as shown in Fig. 4(d).

D. Two bubbles with different radii

The NAC model unavoidably includes the coarsening process by which the smaller bubbles eventually disappear when bubbles of different sizes coexist [30]. This property has often been used to validate the numerical simulations of NAC models in various studies [31,40]. The coarsening phenomenon is undesirable in two-phase fluid flows that do not involve a phase separation or have a low solubility condition. Thus, the proposed LHAC model intended to suppress the prescribed loss of small features during the flow simulation, and it was implemented to retain bubbles with different sizes for sufficient simulation time. In the test of two bubbles with different radii, the LHAC model was compared with the GHAC and

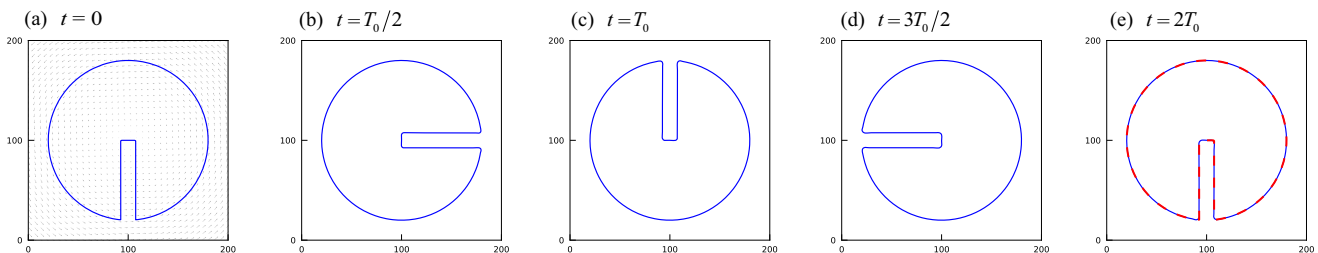


FIG. 3. Rotation of Zalesak’s disk at $Pe = 60$. Blue and red lines represent the final and initial configurations, respectively.

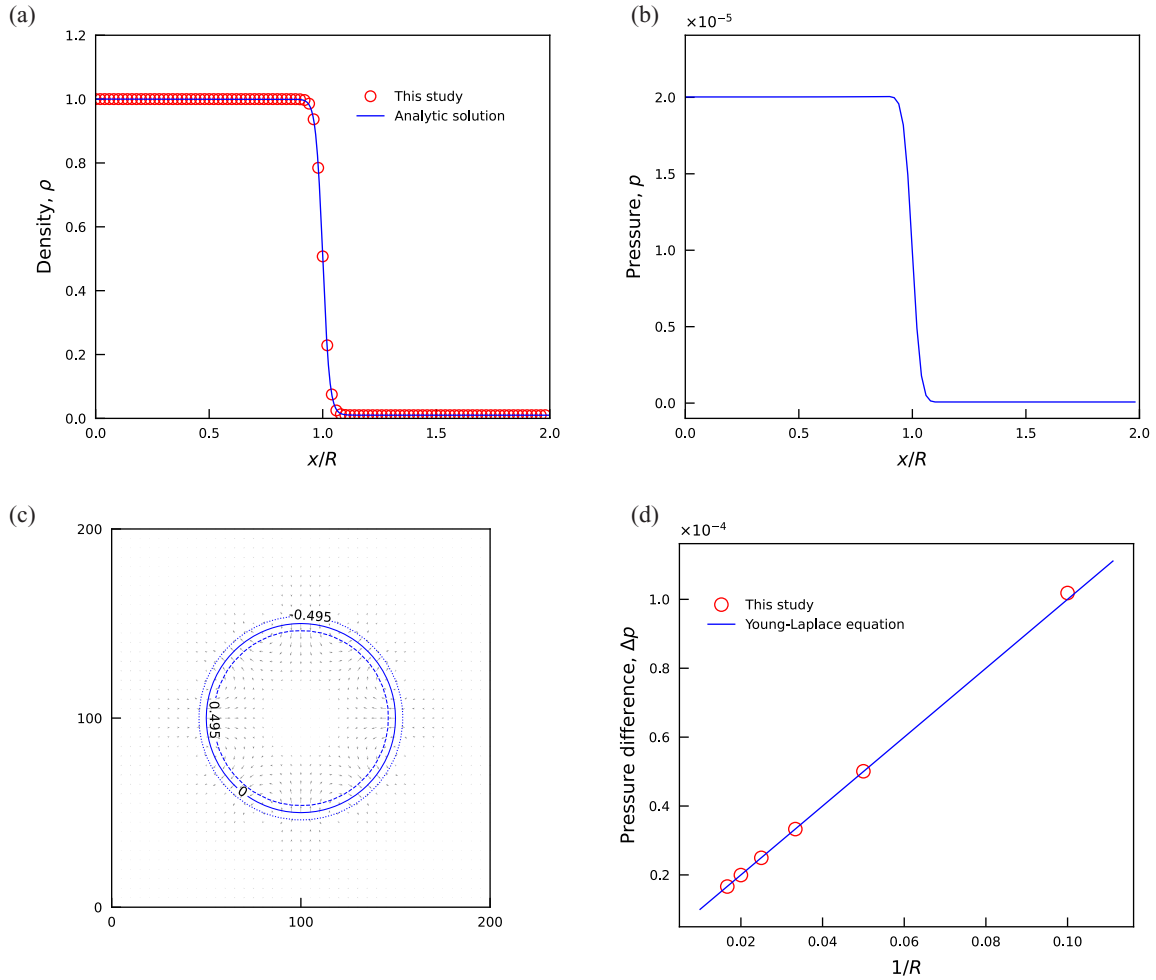


FIG. 4. Static bubble test: (a) density profile, (b) pressure profile, and (c) spurious velocity field ($|\mathbf{u}_{\max}| \approx 2.6 \times 10^{-6}$) with bubble configurations ($\phi = -0.495, 0,$ and 0.495) for $R = 50$. (d) Comparison of estimated pressure difference and Young-Laplace equation.

LAC models, which were implemented by applying the global weights $\lambda = 0.9$ and $\lambda = 1$, respectively. $\delta\phi_{\max}$ is measured as follows:

$$\delta\phi_{\max}(t) = \max(|\phi(\mathbf{x}, t) - \text{sign}(\phi(\mathbf{x}, t))0.5|) \text{ for } \mathbf{x} \in \Omega_B(t). \tag{56}$$

Two bubbles with different radii were initially placed in a domain of $L_0 = 300$. σ , M_ϕ , and τ were chosen as 0.01, 1/6, and 0.53, respectively. The densities of red and blue fluids were set as $\rho_R = 1$ and $\rho_B = 0.1$, respectively. The initial configuration of the order parameters was given as follows:

$$\phi(\mathbf{x}, t = 0) = -\frac{1}{2} \left(\tanh\left(\frac{2}{W}(|\mathbf{x} - \mathbf{x}_1| - R_1)\right) + \tanh\left(\frac{2}{W}(|\mathbf{x} - \mathbf{x}_2| - R_2)\right) - 1 \right), \tag{57}$$

where R_1 and R_2 are $0.1L_0$ and $0.15L_0$, respectively. \mathbf{x}_1 and \mathbf{x}_2 are $(0.25L_0, 0.25L_0)$ and $(0.57L_0, 0.57L_0)$, respectively.

The simulation was conducted for sufficiently large iteration numbers up to approximately 10^6 , while the iterations in the GHAC and LAC models stopped earlier, as the simulations

became trivial or inaccurate. Figure 5 shows the order parameter distribution and interface lines ($\phi = 0$) for different times. The evolution of bubble radii over time is plotted in Fig. 6(a). For the GHAC model, the smaller bubble gradually shrank while the larger one enlarged [see Fig. 6(a)]. Noteworthy, the volume increase for the larger bubble was equivalent to the volume decrease for the smaller bubble, which eventually disappeared before $t = 10^5$. Additionally, the center of each bubble did not change with increasing iteration number. The results of the LAC model simulation indicated that the radii of both bubbles were approximately conserved during the iterations [see Fig. 6(a)]. With increasing time, tiny speckles emerged inside the bulk phases. Figure 6(b) shows the evolution of $\delta\phi_{\max}$ over time. $\delta\phi_{\max}$ almost remained approximately 0.005, and this value corresponds to $\frac{1}{2} - \psi$. This implies that the order parameter fluctuation inside the bulk phase owing to the numerical dispersion exceeds the criterion of a definite interface region. Furthermore, both smaller and larger bubbles moved along left-bottom and right-bottom directions [see Fig. 5(b)]. Noteworthy, all side boundaries were subjected to a periodic condition. This kind of isotropy problem is fundamentally initiated by the asymmetric order in floating-point arithmetic operations [42]. The numerical dispersion

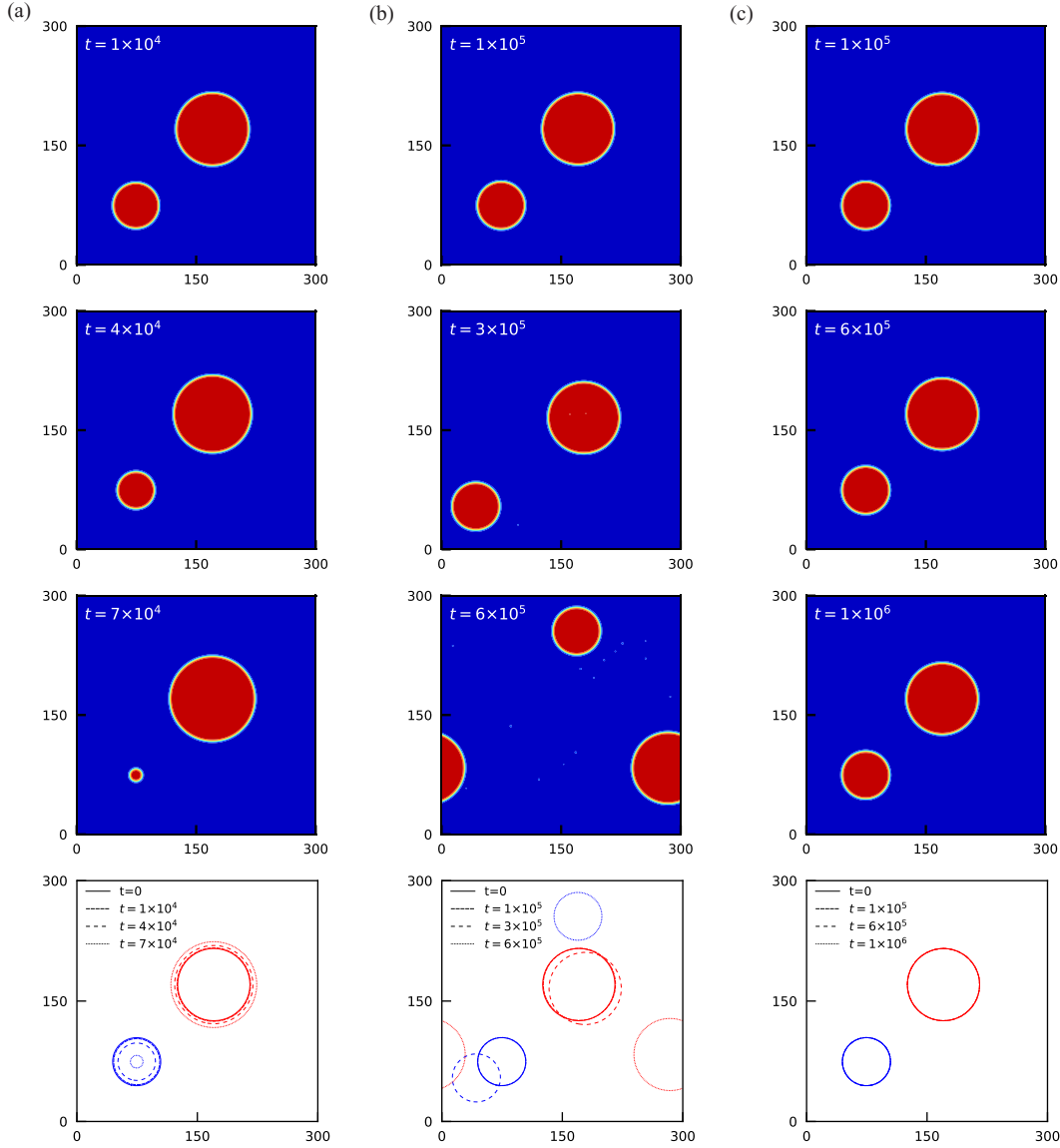


FIG. 5. Evolution of two circles under different weighting schemes: (a) GHAC model ($\lambda = 0.9$), (b) LAC model ($\lambda = 1$), and (c) LHAC model ($\lambda_B=0.9$). The spatial configuration of the order parameter (ϕ) (first three rows) and the corresponding interface lines ($\phi = 0$) are illustrated. Note that all side boundaries are subjected to a periodic condition.

in the LAC model would accelerate the amplification of the artifact owing to the negative feedback by the unexpected surface tension force near speckles. Although this artifact may be insignificant in case of a short simulation time, it would critically affect the numerical accuracy and stability in the case of a long simulation time, such as in a simulation of CO₂ injection into porous media with low capillary numbers. In the LHAC model, the radii and positions of both bubbles were well maintained, and no new speckle was observed during the simulation [see Figs. 5(c) and 6(a)]. The relative evolution of R_1 (i.e., small bubble) was only -0.1% at $t = 10^6$. $\delta\phi_{\max}$ gradually decreased and then remained approximately 5×10^{-6} after $t = 10^5$ [see Fig. 6(b)]. In Appendix, Sec. 1, we present the analytical solution of the bubble radii evolution in the two-bubbles test, and the LB simulation results of the GHAC and LHAC models were well consistent with the analytical solution.

To assess the effect of λ_B , we additionally conducted the two-bubbles test by the LHAC model for different λ_B values as 0, 0.1, 0.3, 0.5, 0.7, 0.9, and 0.99. The simulations also finished at $t = 10^6$. Figure 6(c) presents the relative evolution of bubble radii at $t = 10^6$ against the initial bubbles. As λ_B increased, the relative evolution of bubble radii decreased. The maximum and minimum magnitudes of the relative evolution of R_1 were -0.21% at $\lambda_B = 0.1$ and -0.084% at $\lambda_B = 0.99$, respectively. Figure 6(d) presents $\delta\phi_{\max}$ at $t = 10^6$ for different λ_B values. As λ_B increased, $\delta\phi_{\max}$ increased but was still below 10^{-5} . If λ_B was in the range from 0 to 0.99, then the relative evolution of R_1 and value of $\delta\phi_{\max}$ by the LHAC model were in a sufficiently acceptable range compared to the other models. Therefore, this validation shows that the coarsening process and numerical dispersion can be sufficiently suppressed in the LHAC model compared to the GHAC and LAC models.

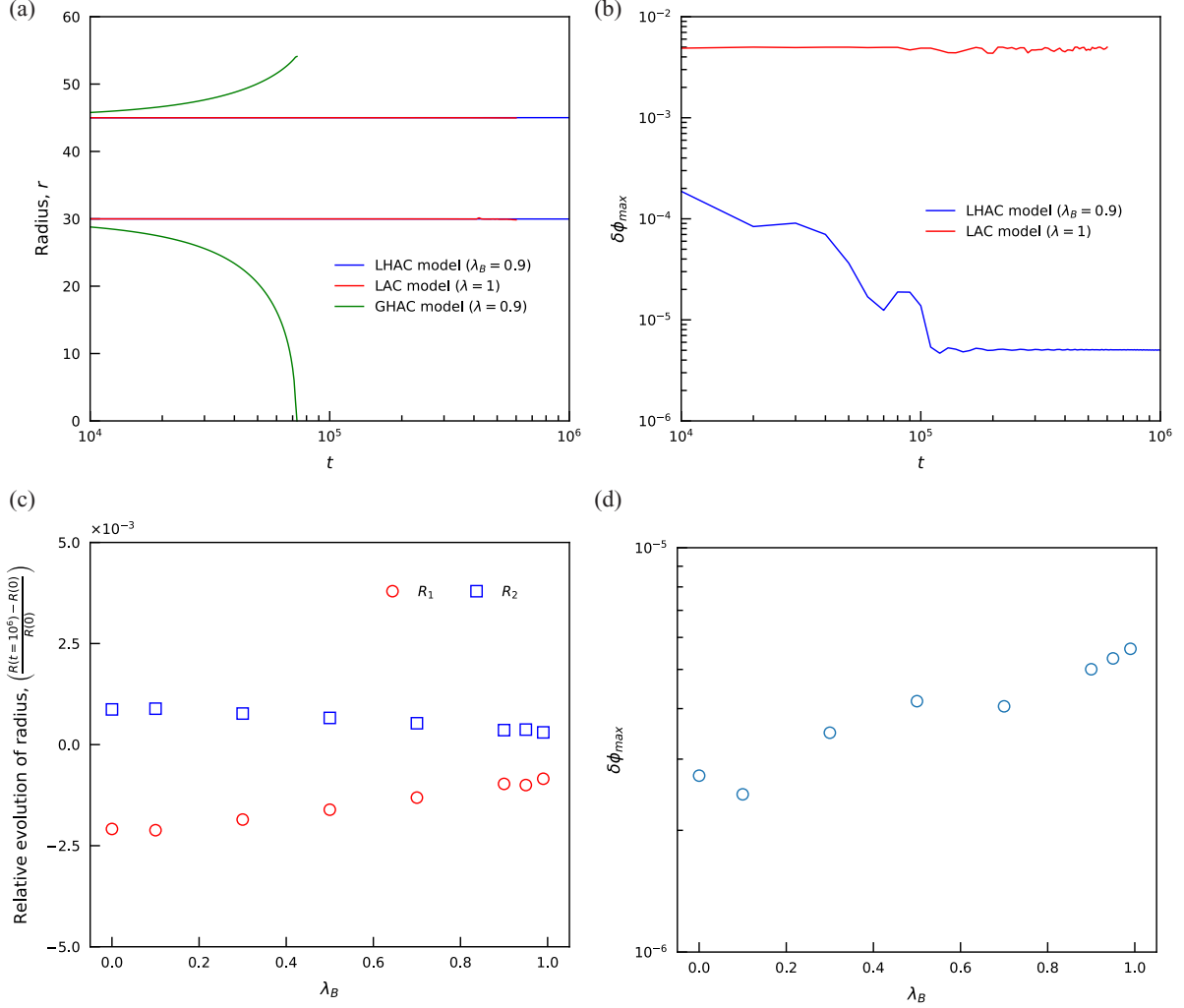


FIG. 6. Comparison of LHAC model with other models in evolution of (a) radii of bubbles and (b) the largest value of the fluctuation of the order parameter $\delta\phi_{\max}$ in Ω_B for time. Effect of λ_B in LHAC model: (c) evolution of radii of bubbles and (d) $\delta\phi_{\max}$ at $t = 10^6$.

E. RTI problem

In the previous two tests, the numerical dispersion induced by spurious velocity was considered without complex interface dynamics. To evaluate the performance of the proposed HAC model in more complex interface dynamics with suppressing $\delta\phi_{\max}$, the RTI test, which has been frequently used in the validation of two-phase LB models [19,20,43,44], was conducted. RTI, a fundamental interface instability, occurs when a heavier fluid resides on a lighter one. The density difference and a small perturbation of the interface result in characteristic flow behavior over several stages, which eventually develops towards a chaotic state [45]. Three dimensionless numbers, Atwood number (A), Péclet number (Pe), and Reynolds number (Re), are usually used to demonstrate the flow characteristics in RTI as follows:

$$A = \frac{\rho_R - \rho_B}{\rho_R + \rho_B}, \quad Pe = \frac{\lambda_0 \sqrt{gL_0}}{M_\phi}, \quad \text{and} \quad Re = \frac{L_0}{\nu} \sqrt{\frac{AgL_0}{1+A}}, \quad (58)$$

where g is a gravitational acceleration.

The domain size was set as $L_0 \times 4L_0$, and a solid wall was placed at the top and bottom sides. A periodic condition

was imposed on the left and right boundaries. The initial configuration of ϕ was given as follows:

$$\phi(x, y, 0) = -\frac{1}{2} \tanh \left(2L_0 + 0.05L_0 \cos \left(\frac{2\pi x}{\lambda_0} \right) - y \right) \times \text{in} (x, y) \in [0, L_0] \times [0, 4L_0] \quad (59)$$

where λ_0 represents wavelength of the phase interface for imposing the initial perturbation.

The hydrostatic pressure at the initial state was expressed as follows:

$$p(x, y, 0) = g \int_y^{4L_0} \rho(x, y, 0) dy. \quad (60)$$

The simulation parameters were chosen as $L_0 = \lambda_0 = 256$, $\sqrt{gL_0} = 0.04$, $\sigma = 5 \times 10^{-5}$, $Pe = 1000$, $A = 0.1$, and $\rho_R = 1$. The validation was conducted for different Re values of 30, 150, and 3000. The spatial configuration of ϕ and corresponding Ω_I are presented for a normalized time $t^* = t\sqrt{Ag/\lambda_0}$ in Fig. 7. Once the simulation started, the heavy (red) fluid gradually penetrated the light (blue) one along the centerline by forming a mushroom shape from its initial finger shape.

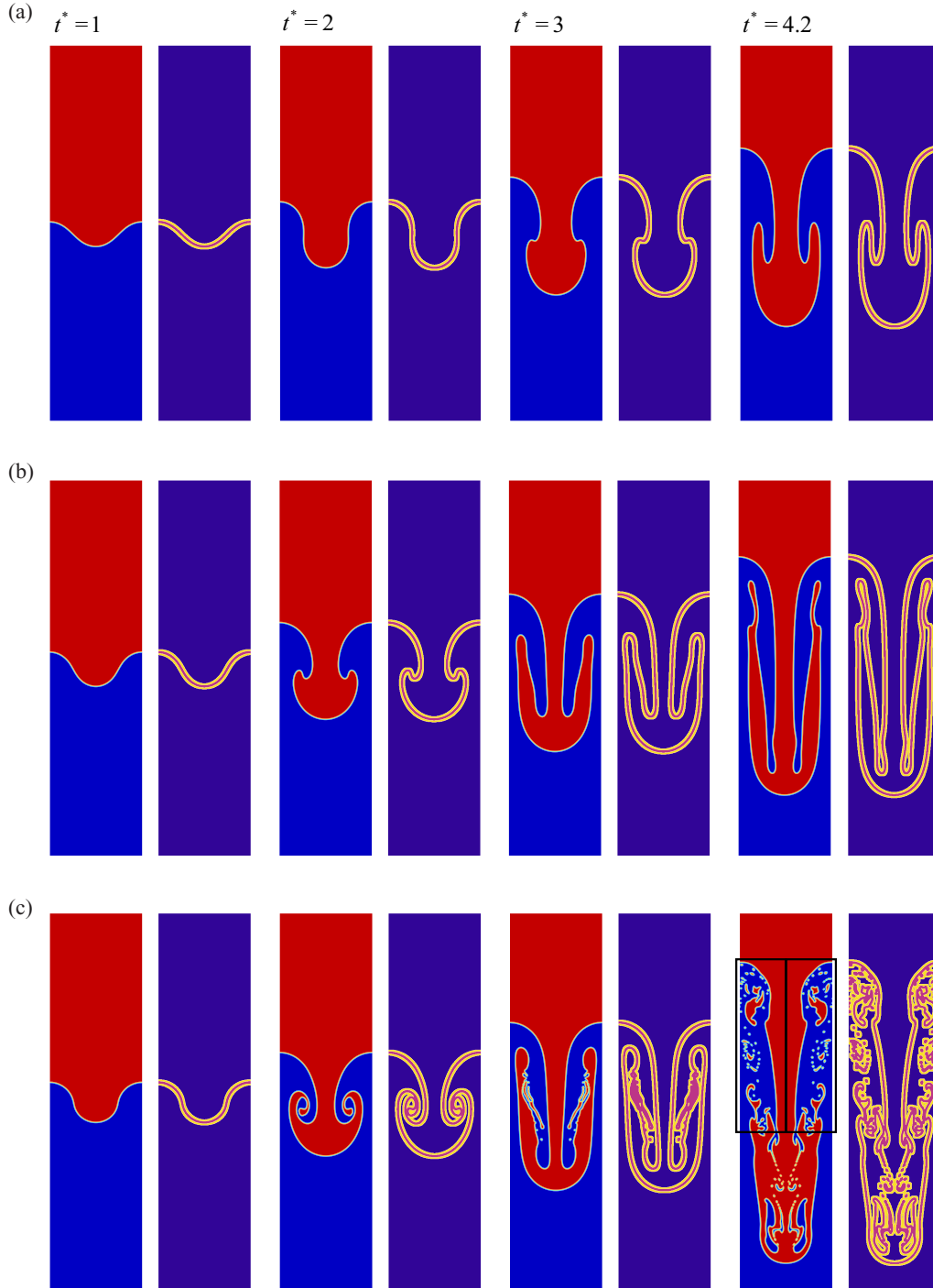


FIG. 7. Phase distribution (left) and interface region Ω_I (right) in the RTI tests for different normalized times under $Re =$ (a) 30, (b) 150, and (c) 3000. In the captured interface map, the reddish color indicates $\hat{\Omega}_I$.

Simultaneously, the bubble of the light fluid raised beside the finger of the heavy fluid. As Re increased [see Figs. 7(a) and 7(b)], the pileus stretched more from the front of the spike to the rising bubble over time. As Re further increased [see Fig. 7(c)], the induced vorticity broke continuously developed phases by a single interface before the chaotic stage and then the broken small speckles penetrated the rising bubbles and falling spike chaotically. Among cases, the interface region

Ω_I was well outlined, and the order parameter ϕ for each fluid was uniformly distributed in Ω_B during the complex interface motions. The front positions in the spike of the heavy fluid ($y < 2L_0$) and bubble of the light fluid ($y > 2L_0$) were fairly consistent with those in a previous study that used the CH model under the same conditions [20] for different Re values, as shown in Fig. 8(a). $\delta\phi_{\max}$ exceeded 10^{-4} after $t^* = 1-1.3$ but was under 10^{-3} ($< \frac{1}{2} - \psi$) [see Fig. 8(b)]. For $Re = 3000$

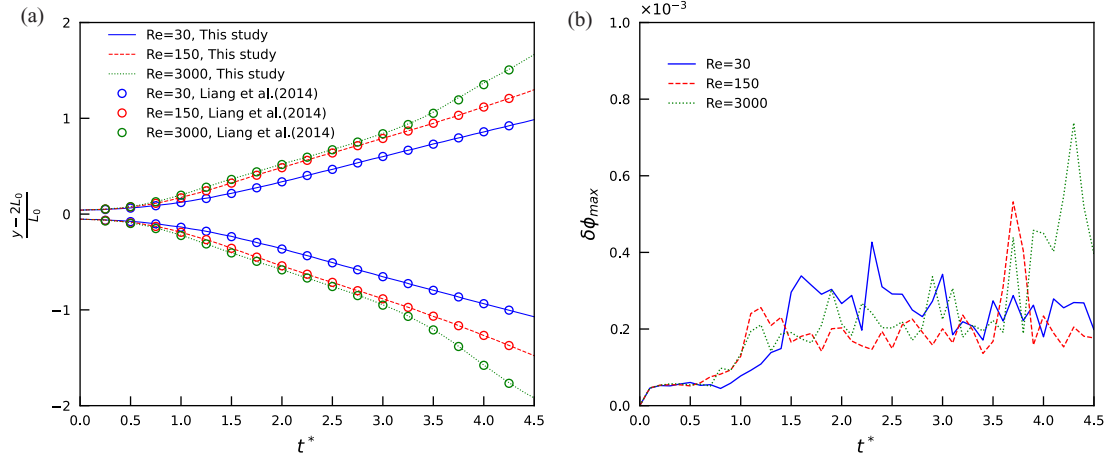


FIG. 8. (a) Evolution of front positions in a rising bubble and a sinking spike. (b) The largest value of the fluctuation of the order parameter $\delta\phi_{\max}$.

and $t^* = 4.2$, a small violation of symmetry in the spatial distribution of ϕ was observed in the rising bubble regions [see inside two boxes of black lines in Fig. 7(c)]. The asymmetry is essentially attributed to asymmetric order in floating-point arithmetic operations in the numerical simulation [42]. Generally, diffusion reduces instability growth rate [46]. Although asymmetry was not achieved under the same conditions as those in the previous study [20], the local spreading of ϕ near the interface was pronounced. Thus, compared with the previous study, the stronger antidiffusion nature preserving the interface thickness and suppressing the numerical dispersion in the LHAC model might amplify the asymmetry. Nevertheless, the results of the RTI simulation support that the LHAC model is adequately accurate and stable at some level of complex interface dynamics.

IV. IMMISCIBLE FLUID INJECTION SIMULATION

The numerical stability improved by the proposed model allows conducting flow simulations of immiscible fluid injection (e.g., CO₂ storage study) through porous media that involve complex pore geometry, inlet-outlet boundary conditions, and large simulation time.

The injected and displaced fluids were supercritical carbon dioxide (SCO₂) and brine, respectively, whose pressure and temperature condition were chosen as 7.45 MPa and 35 °C, respectively [47]. Two-dimensional porous media were constructed by modifying an x-ray computed tomographic image of Ottawa 20–30 sand by image processing such as binarization, watershed, and morphological erosion of randomly selected solid grains [see Fig. 9(a)]. The inlet comprised a bundle of 50 injection holes ($N_{in} = 50$) and a buffer zone in series. The height of the flow domain had 1176 pixels. Each injection hole had 20×50 pixels [see Fig. 9(b)]. The buffer and porous zones had widths of 250 and 3224 pixels, respectively. The image resolution was $5 \mu\text{m}/\text{pixel}$. The impermeable solid walls were set to the top and bottom sides of the domain. SCO₂ was injected at a volumetric flow rate Q into the domain. For that, the individual injection pressure $p_{in}^{(a)}$ imposed at the a th injection hole was calculated according to Appendix, Sec. 2, to meet the volumetric flow rate at the hole, $Q_{in}^{(a)} (= Q/N_{in})$ [see Fig. 9(b)]. In our experience, reentrant flow can sometimes occur near the inlet boundary even in satisfying the target volumetric flow rate, if applying a single injection pressure value to the inlet plane without injection hole structure. This reentrant flow increases the local velocity and then reduces the numerical stability of the LB simulation.

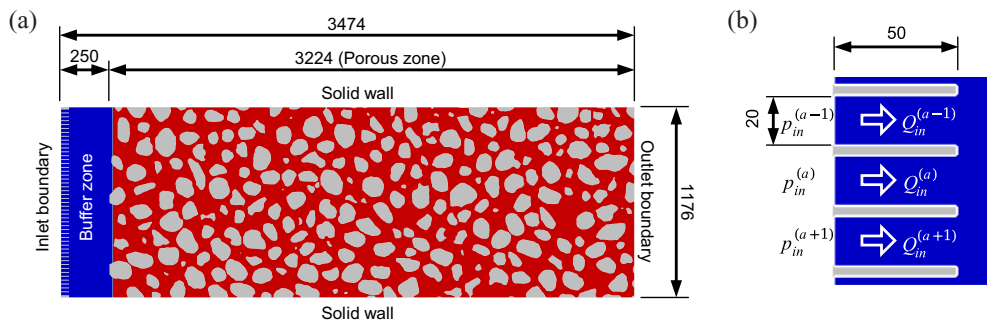


FIG. 9. (a) Initial configuration of drainage simulation [red: brine (wetting fluid), blue: SCO₂ (nonwetting fluid), gray: solid]. (b) Nonwetting fluid is injected through injection holes placed at serration grooves on the left side. Wetting fluid outflows through the right outlet boundary where pressure is constrained constantly. The top and bottom boundaries are sealed by solid walls.

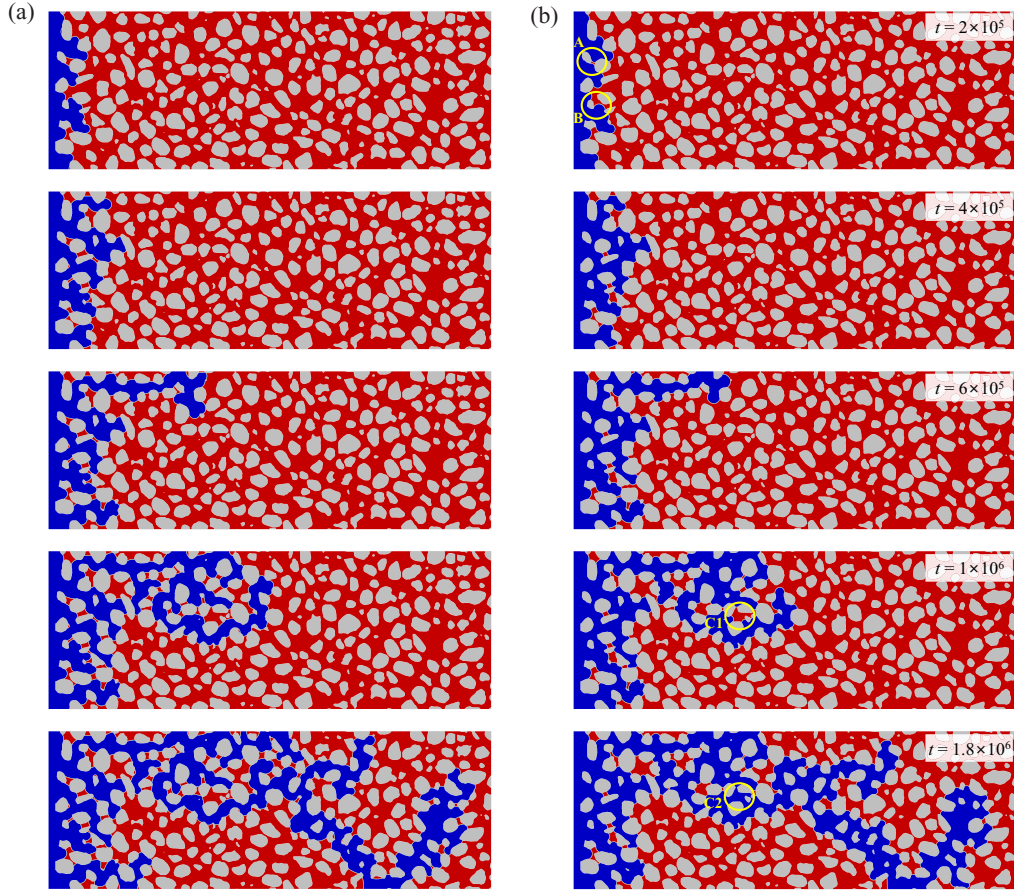


FIG. 10. Evolution of injected and displaced fluid configurations in the (a) LHAC and (b) GHAC models for $t(10^5) = 2, 4, 6, 10,$ and 18 .

To prevent that, in this study, the injection boundary plane was forcibly partitioned into multiple injection holes via which SCO_2 could be uniformly injected. Additionally, the constant order parameters of SCO_2 ($\phi = -0.5$) and brine ($\phi = 0.5$) were imposed to the inlet and outlet boundaries during the simulation. The detailed implementation is described in Appendix, Sec. 2.

The properties of each fluid in the physical and LB systems used in this study are presented in Table I. Hereinafter, the values of quantities follow the LB unit system, and the units are omitted, unless specified. The order parameter at the solid wall, ϕ_{wall} , was determined by a geometrical formulation with a weighted averaging scheme for a directional derivative to impose the target contact angle θ [14]. The dimensionless capillary number was $Ca = \frac{\mu_{\text{CO}_2} U_{\text{CO}_2}}{\sigma} = 10^{-5}$ at which U_{CO_2}

denotes the Darcy velocity of SCO_2 over the flow domain. U_{CO_2} , Q , and $Q_{\text{in}}^{(a)}$ were 4.925×10^{-4} , 0.5792 , and 0.0116 , respectively. M_ϕ and W were $1/6$ and 3 , respectively. The pore space in the inlet zone and the porous zone was initially filled by SCO_2 (nonwetting fluid) and brine (wetting fluid), as shown in Fig. 9. For comparison, the injection simulation was conducted by the LHAC and GHAC models. The simulation continued until the front of the injected SCO_2 reached the outlet boundary.

Figures 10(a) and 10(b) show the evolutions of injected SCO_2 (blue) and displaced brine (red) at $t = 2, 4, 6, 10,$ and 18×10^5 time steps in the LHAC and GHAC models. Noteworthy, the overall invasion patterns of SCO_2 were similar in both models during the simulations. As the injection continued, SCO_2 invaded in the form of a common capillary

TABLE I. Fluid properties used in the drainage simulation (pressure: 7.45 MPa, temperature: 35 °C).

	Physical system		LB system	
	Brine (<i>R</i>)	SCO_2 (<i>B</i>)	Brine (<i>R</i>)	SCO_2 (<i>B</i>)
ρ	1000 kg/m ³	348 kg/m ³	1	0.348
μ	7.1×10^{-4} Pa · s	2.8×10^{-5} Pa · s	8.3333×10^{-3}	3.2864×10^{-4}
σ	23.5 mN/m		1.6187×10^{-2}	
θ^{eq}			30°	

fingering pattern such that many patches of brine surrounded by the fingers and solid grains were trapped. However, detailed differences between both models can be easily observed in Fig. 10. As intended, in the proposed model, the trapped patches of brine were almost preserved during the injection time unless they were displaced. In the GHAC model, contrarily, some of the trapped patches disappeared by the coarsening process during the simulation. For instance, at the early stage ($t = 2 \times 10^5$), as the volume of brine trapped between grains shrank (in yellow circle A), SCO_2 filled that space so that the other finger of SCO_2 (in yellow circle B) less invaded an equivalent amount of brine. At the breakthrough time, many of the small patches disappeared. Overall, the large patches survived more than small patches. In the multiple bubbles test (see Sec. III D), compared with larger bubbles, smaller bubbles tended to disappear more rapidly; this is because bubbles are perfectly spherical, and the rate of the coarsening process depends on the interfacial curvature of an object. In this simulation, the interfacial curvature was affected by the interaction of pore structure, contact angle, and dynamic motions. Accordingly, a patch larger than other surviving small patches disappeared by the coarsening phenomenon (in yellow circles C1 and C2). Consequently, the front of the invading SCO_2 reached the outlet boundary slightly faster in the LHAC model than in the GHAC model because brine was more trapped in form of patches in the LHAC model. Conversely, the GHAC model tends to overestimate the saturation of SCO_2 at the breakthrough.

V. SUMMARY

In previous phase-field LB models based on the LAC or NAC or GHAC model, the numerical dispersion or the coarsening phenomenon was an obstacle in the study of incompressible two-phase fluid flows. To counter this drawback, we introduced the LHAC model in the phase-field LB model. The local weights for the LAC and NAC source terms were differently applied to the interface and bulk phase regions, which were determined by applying binary thresholding and morphological dilation to the spatial distribution of the order parameter. To validate the LHAC model, we used five standard benchmarks. The results in the interface tracking and the hydrodynamics were sufficiently correct. Additionally, the numerical dispersion and the coarsening phenomenon were considerably reduced compared with the LAC and GHAC models, respectively. Moreover, to test the performance in porous media flows, a drainage simulation of SCO_2 in a heterogeneous pore structure saturated by brine was conducted by the LHAC and GHAC models. The SCO_2 invasion followed the capillary fingering pattern in both models, and the overall features were similar to each other. However, owing to the coarsening phenomenon, the brine patches trapped between grains were fairly underestimated in the GHAC model, but the LHAC model could correctly depict them. This result supports that the proposed LHAC model can somewhat preserve small features in the long-time simulation of two-phase fluid flows such as a drainage process under low capillary number.

ACKNOWLEDGMENT

This work was supported by the National Research Foundation of Korea (NRF) grant funded by the Korea government (MSIT) (Grants No. 2019R1A6A3A03032835, No. 2020R1A2C1014815, No. 2021R1I1A1A01060210, and No. 2021R1A5A1032433).

The authors declare that they have no known competing financial interests or personal relationships that could have influenced this work.

D.H.K. contributed conceptualization, methodology, validation, investigation, writing, and funding acquisition; T.S.Y. contributed supervision, writing review and editing, and funding acquisition.

APPENDIX

1. Analytical solution of multiple bubbles system in LHAC and GHAC models

While the source term of the LAC model D_L is conservative, the source term of the NAC model D_{NL} is only globally conservative but locally nonconservative, which causes the coarsening process. This section validates that the LHAC model can better mitigate the coarsening process than the GHAC model by comparing the mass transfer rates from a small bubble to a large bubble.

The flow is set to a stationary condition [i.e., $\mathbf{u}(\mathbf{x}) = \mathbf{0}$] and a bubble of a radius R_j is exclusively placed in a subdomain $\bar{\Omega}_j$. Herein, the subscript j indicates the j th bubble in N bubbles. The analytical solution of the order-parameter profile of the j th bubble, ϕ_j , can be approximated in the form of a hyperbolic tangent function as Eq. (55) for both the LAC and NAC models. So, ϕ_j in the GHAC model also has the same form by the linearity. Similarly, in the LHAC model, let us suppose the interface configuration of the j th bubble having the radius R_j in the subdomain $\bar{\Omega}_j$ practically follows the equilibrium profile of the order parameter ϕ_j as

$$\phi_j(r, t) = -\frac{1}{2} \tanh\left(\frac{2}{W}(r - R_j(t))\right) \text{ for } \mathbf{x} \in \bar{\Omega}_j \text{ and } r = |\mathbf{x}|, \quad (\text{A1})$$

where r is a distance from the center of $\bar{\Omega}_j$ and \mathbf{x} are the local coordinates in $\bar{\Omega}_j$.

In the LHAC model, even though some discontinuity of the order parameter occurs in an instant by the discontinuous weight Λ for the source terms under the coarsening process, they might be diffused and converge to the equilibrium profile quickly. For the sake of simplicity in the volume integral, the subdomain $\bar{\Omega}_j$ was assigned to a bounded set that is a circular one of diameter L_j as $\bar{\Omega}_j = \{\mathbf{y} | |\mathbf{y}| \leq L_j/2\}$. It is also assumed that the subdomains are independent of each other except for the Lagrange multiplier λ , which is shared over the entire domain $\bar{\Omega} (= \bar{\Omega}_1 \cup \bar{\Omega}_2 \cup \dots \cup \bar{\Omega}_N)$ for the global mass conservation. In other words, all subdomains $\bar{\Omega}_j$ are disjoint sets. The instantaneous change rate of the order parameter by the source terms just prior to the diffusion process under the stationary condition can be yielded from Eq. (3) as

$$\begin{aligned} \frac{\partial \phi_j}{\partial t} = D_{NL,j} &= (1 - \Lambda_j) M_\phi \frac{32\phi_j(\frac{1}{2} + \phi_j)(\frac{1}{2} - \phi_j)}{W^2} \\ &+ \gamma(\frac{1}{2} + \phi_j)(\frac{1}{2} - \phi_j) = (1 - \Lambda_j)a_j + \gamma b_j. \end{aligned} \quad (\text{A2})$$

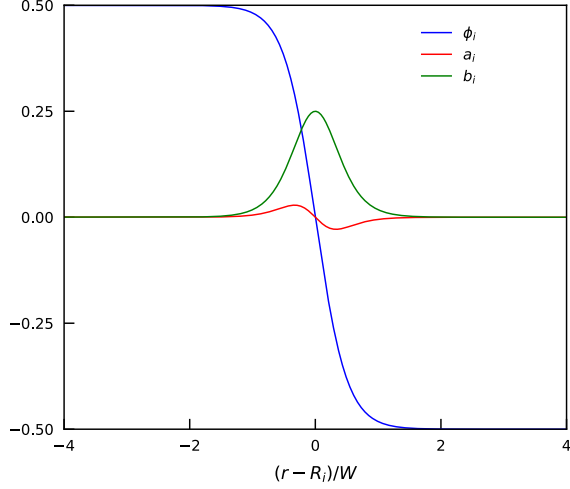


FIG. 11. One-dimensional profiles of ϕ_j , a_j , and b_j for a bubble with $R_j = 30$, $M_\phi = \frac{1}{16}$, and $W = 3$.

Figure 11 illustrates the 1D profiles of ϕ_j , a_j , and b_j across the interface and bulk fluid regions for a bubble with $R_j = 30$, $M_\phi = 1/6$, and $W = 3$. It is obvious that the magnitude of the linear combination of a_j and b_j , which is the source of non-conservation in local mass is higher in the interface region Ω_I than in the bulk phase region Ω_B . This implies the source term of the NAC model should be excluded in Ω_I to suppress the coarsening process. After applying the above source term, the order parameter $\phi_j(r, t + \delta t)$ follows the equilibrium profile corresponding to the updated bubble radius $R_j(t + \delta t)$.

The volume integral of $\phi_j(r, t)$ over the sub-domain $\bar{\Omega}_j$ is expressed as

$$\begin{aligned} \Theta_j(t) &= \Theta_j(R_j(t)) = \int_{\bar{\Omega}_j} \phi_j dV = \int_0^{L_j/2} 2\pi r \phi_j(r, t) dr \\ &= E_j(L_j/2, t) - E_j(0, t), \end{aligned} \quad (\text{A3})$$

with

$$\begin{aligned} E_j(x, t) &= \frac{\pi}{8} (W^2 \text{Li}_2(-e^{(4/W)\{[R_j(t)-x]\}}) \\ &\quad - 4\pi W x \ln(e^{(4/W)\{[R_j(t)-x]\}} + 1) - 4\pi x^2), \end{aligned} \quad (\text{A4})$$

where Li_2 is Spence's function.

By the volume integral of Eq. (A2), the change rate of Θ_j is also obtained as

$$\frac{\partial \Theta_j}{\partial t} = \dot{\Theta}_j = \int_{\bar{\Omega}_j} D_{NL,j} dV = A_j + \gamma B_j, \quad (\text{A5})$$

where

$$\begin{aligned} A_j(t) &= \frac{2\pi M_\phi (1 - \lambda_B)}{W} \left(\frac{W - 4\xi e^{-(2\xi/W)} - W e^{-(4\xi/W)}}{1 + e^{-(4\xi/W)} + 2e^{-(2\xi/W)}} \right. \\ &\quad \left. - \frac{W}{1 + e^{-\{[4R_j(t)]/W\}}} + \frac{(W + 2L_j)e^{\frac{2}{W}(L_j - 2R_j(t))} + W}{1 + 2e^{\frac{2}{W}(L_j - 2R_j(t))} + e^{-\{[4L_j]/W\}}} \right), \end{aligned} \quad (\text{A6})$$

$$\begin{aligned} B_j(t) &= \frac{\pi W^2}{8} \ln \frac{(1 + e^{-\{[4R_j(t)]/W\}})}{(1 + e^{\frac{2}{W}(L_j - 2R_j(t))})} \\ &\quad + \frac{\pi W}{4} \frac{L_j}{(1 + e^{-\frac{2}{W}(L_j - 2R_j(t))})}, \end{aligned} \quad (\text{A7})$$

$$\gamma(t) = - \frac{\sum_{j=1}^N A_j(t)}{\sum_{j=1}^N B_j(t)}. \quad (\text{A8})$$

We evaluated $\Theta_j(t + \delta t)$ from $\Theta_j(t)$ by the time integral to Eq. (A5) by the Dormand-Prince method and then found $R_j(t + \delta t)$ satisfying Eqs. (A3) and (A4) for the obtained $\Theta_j(t + \delta t)$ via a root-finding method. Repeating the above procedures, we could analytically evaluate the change of bubble radii for given ξ .

As in Sec. III D, the analytical solution for the two-bubbles test was examined. The seven values of ξ uniformly selected as 0, 3, ..., and 18 were used to show how more effectively the LHAC model mitigates the coarsening process than the GHAC model. Other parameters are identical to the values of the previous example. Note that ξ for $\Delta_\xi = 10^{-5}$ in Sec. III D is approximately 17.27. Figure 12(a) presents the evolution of R_1 for time t ranged in 10^4 – 10^8 in the analytical solution of the two-bubbles test. The line of $\xi = 0$ corresponds to the GHAC model. The analytical solution of $\xi = 0$ was in good agreement with the LB simulation result. This implies that the LB schemes do not affect the coarsening process, which is just a fundamental nature in the NAC source term. As expected, it was obtained that the greater the ξ , the smaller the shrinkage rate of the small bubble. The LB simulation result of the LHAC model obtained in Sec. III D is placed near the line of $\xi = 18$. The relative evolution of R_1 at $\xi = 18$ was -0.059% at $t = 10^6$. This is well consistent with -0.1% of the LB simulation result. Furthermore, it was observed that the shrinkage of the small bubble for $\xi \geq 6$ stops at a certain critical radius $R_{\text{crit},1}$ whereas the bubbles for $\xi = 0$ and 3 finally disappear. The critical radius $R_{\text{crit},1}$ of bubble 1 satisfies following condition:

$$\dot{\Theta}_1(R_{\text{crit},1}) = 0 \text{ and } R_{\text{crit},1} > 0. \quad (\text{A10})$$

Instead of solving Eq. (A10) directly, we obtained the linear relation of $R_{\text{crit},1}$ for ξ by the least-square fitting for the computed four points in $\xi = 6$ – 15 as shown in Fig. 12:

$$\frac{R_{\text{crit},1}}{W} = 0.45343 \left(\frac{\xi}{W} \right) - 0.51599 \quad \text{with } R^2 = 0.99999 \quad (\text{A11})$$

Extrapolating Eq. (A11), we can conclude that bubble 1 may survive after $\xi = 3.4139$ at the given two-bubbles test condition. Although the LHAC model cannot completely eliminate the coarsening process, the rate of unwanted mass transfer is substantially reduced enough on the LB simulation timescale.

2. Implementation of boundary conditions at the open boundary

For the hydrodynamic LB part, we applied the inflow boundary condition for determining unknown f_i at the inlet boundary $\Gamma_{in} (= \Gamma_{in}^{(1)} \cup \Gamma_{in}^{(2)} \cup \dots \cup \Gamma_{in}^{(N_{in})})$ after the streaming step. Kang *et al.* [14] introduced the inflow boundary that can

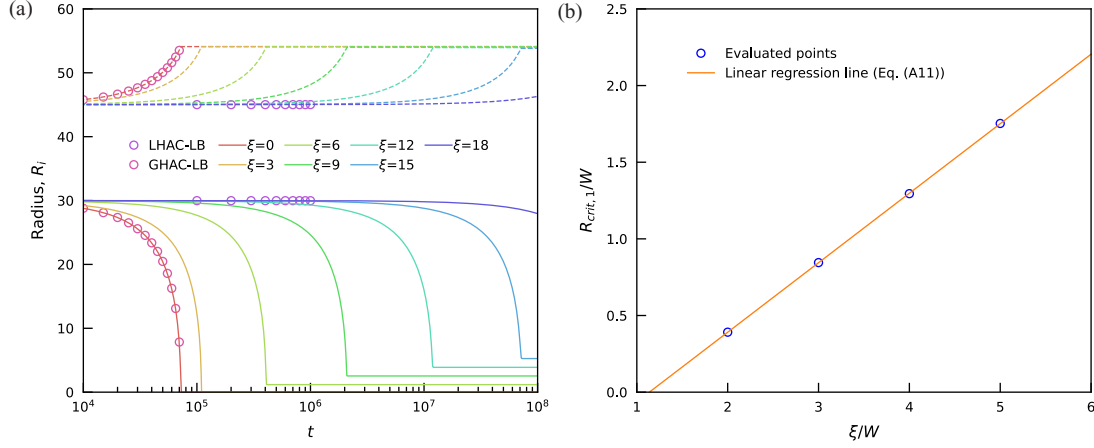


FIG. 12. (a) Analytical solution of bubble radii evolution in the two-bubbles test with different ξ values and (b) critical radius of the small bubble for ξ .

attain a target volumetric flow rate by manipulating the inlet pressure using the nonequilibrium part bounceback (NEBB) scheme for the pressure boundary proposed by Zou and Hu [48]. Suppose that no surface tension force and density gradient are at the a th inlet boundary plane $\Gamma_{in}^{(a)}$, the inlet pressure $p_{in}^{(a)}$ is uniform, the volumetric flow rate is $Q_{in}^{(a)}$, and the normal direction vector outward the domain is \mathbf{n}_b . An averaged particle distribution function $\bar{f}_i^{(a)}$ at the inlet boundary $\Gamma_{in}^{(a)}$ is given as follows:

$$\bar{f}_i^{(a)} = \frac{1}{A_{in}^{(a)}} \sum_{\mathbf{x} \in \Gamma_{in}^{(a)}} f_i(\mathbf{x}), \quad (\text{A12})$$

where $A_{in}^{(a)}$ represents the area of $\Gamma_{in}^{(a)}$.

By taking area averages in Eqs. (46) and (47) over $\Gamma_{in}^{(a)}$, the averaged pressure and momentum can be given as follows:

$$p_{in}^{(a)} \simeq \frac{c_s^2}{1 - w_0} \left(\sum_{i \neq 0} \bar{f}_i^{(a)} + \rho_{in} s_0(\bar{\mathbf{u}}^{(a)}) \right), \quad (\text{A13})$$

$$\rho_{in} \bar{\mathbf{u}}^{(a)} = \sum_i \bar{f}_i^{(a)} \mathbf{e}_i + \frac{\delta t}{2} \bar{\mathbf{F}}_b^{(a)}, \quad (\text{A14})$$

where $\bar{\mathbf{F}}_b^{(a)}$ represents the averaged ‘‘other possible body force’’ acting on $\Gamma_{in}^{(a)}$.

If $\bar{\mathbf{u}}^{(a)}$ has only a velocity component normal to $\Gamma_{in}^{(a)}$ in case the unit normal vector outward from Ω is \mathbf{n}_b , then the normal component in Eq. (A14) is given as follows:

$$\begin{aligned} \rho_{in} \bar{\mathbf{u}}^{(a)} \cdot (-\mathbf{n}_b) &= \rho_{in} \frac{Q_{in}^{(a)}}{A_{in}^{(a)}} = \rho_{in} u_{in}^{(a)} \\ &= - \sum_{i \neq 0} \mathbf{e}_i \cdot \mathbf{n}_b \bar{f}_i^{(a)} - \frac{\delta t}{2} \bar{\mathbf{F}}_b^{(a)} \cdot \mathbf{n}_b. \end{aligned} \quad (\text{A15})$$

The summation of $\bar{f}_i^{(a)}$ for $i > 0$ in Eq. (A13) can be expressed as sum of known and unknown populations after the streaming step. One has

$$\sum_{i \neq 0} \bar{f}_i^{(a)} = \sum_{\substack{i \neq 0 \\ \mathbf{e}_i \cdot \mathbf{n}_b < 0}} \bar{f}_i^{(a)} + \sum_{\substack{i \neq 0 \\ \mathbf{e}_i \cdot \mathbf{n}_b \geq 0}} \bar{f}_i^{(a)}, \quad (\text{A16})$$

where $\bar{f}_i^{(a)}$ for $\mathbf{e}_i \cdot \mathbf{n}_b \geq 0$ and $\mathbf{e}_i \cdot \mathbf{n}_b < 0$ are known and unknown particle distribution functions, respectively, after the streaming step.

Similarly, Eq. (A15) can be expressed as

$$\rho_{in} u_{in}^{(a)} = \sum_{\substack{i \neq 0 \\ \mathbf{e}_i \cdot \mathbf{n}_b < 0}} \bar{f}_i^{(a)} - \sum_{\substack{i \neq 0 \\ \mathbf{e}_i \cdot \mathbf{n}_b \geq 0}} \bar{f}_i^{(a)} - \frac{\delta t}{2} \bar{\mathbf{F}}_b^{(a)} \cdot \mathbf{n}_b. \quad (\text{A17})$$

Equation (A17) is substituted into Eq. (A16) to eliminate the unknown particle distribution functions $\bar{f}_i^{(a)}$ of $\mathbf{e}_i \cdot \mathbf{n}_b < 0$ as

$$\begin{aligned} \sum_{i \neq 0} \bar{f}_i^{(a)} &= \sum_{\substack{i \neq 0 \\ \mathbf{e}_i \cdot \mathbf{n}_b < 0}} \bar{f}_i^{(a)} + \sum_{\substack{i \neq 0 \\ \mathbf{e}_i \cdot \mathbf{n}_b \geq 0}} \bar{f}_i^{(a)} = \sum_{i \neq 0} (1 + \mathbf{e}_i \cdot \mathbf{n}_b) \bar{f}_i^{(a)} \\ &+ \rho_{in} u_{in}^{(a)} + \frac{\delta t}{2} \bar{\mathbf{F}}_b^{(a)} \cdot \mathbf{n}_b. \end{aligned} \quad (\text{A18})$$

Substituting Eq. (A18) into Eq. (A13), the inlet pressure can be calculated to obtain the target volumetric flow rate $Q_{in}^{(a)}$ at $\Gamma_{in}^{(a)}$ as follows:

$$\begin{aligned} p_{in}^{(a)} &= \frac{c_s^2}{1 - w_0} \left(\sum_{i \neq 0} (1 + \mathbf{e}_i \cdot \mathbf{n}_b) \bar{f}_i^{(a)} + \rho_{in} u_{in}^{(a)} \left(1 - w_0 \frac{u_{in}^{(a)}}{2c_s^2} \right) \right. \\ &\left. + \frac{\delta t}{2} \bar{\mathbf{F}}_b^{(a)} \cdot \mathbf{n}_b \right). \end{aligned} \quad (\text{A19})$$

Using the inlet pressure $p_{in}^{(a)}$, unknown particle distribution functions f_i of $\mathbf{e}_i \cdot \mathbf{n}_b < 0$ for each node at $\Gamma_{in}^{(a)}$ can be determined by the NEBB pressure boundary of Zou and He [48].

For the phase-field LB part, the remainder of the order parameter, $\delta_u \phi$, is weighted using the directional weight w_i and is distributed to the unknown g_i to impose the target order parameter ϕ on the open boundary. $\delta_u \phi$, which is the difference between the target order parameter ϕ and the sum of known g_i , is calculated as follows:

$$\delta_u \phi = \phi - \sum_{\mathbf{e}_i \cdot \mathbf{n}_b \geq 0} g_i. \quad (\text{A20})$$

The unknown particle distribution function g_i is then calculated as follows:

$$g_i = \alpha_i \delta_u \phi \text{ for } \mathbf{e}_i \cdot \mathbf{n}_b < 0, \quad (\text{A21})$$

with

$$\alpha_i = \frac{w_i}{\sum_{\mathbf{e}_j \cdot \mathbf{n}_b < 0} w_j}. \quad (\text{A22})$$

- [1] S. Succi, *The Lattice Boltzmann Equation for Fluid Dynamics and Beyond* (Clarendon Press, 2001).
- [2] U. Frisch, B. Hasslacher, and Y. Pomeau, Lattice-Gas Automata for the Navier-Stokes Equation, *Phys. Rev. Lett.* **56**, 1505 (1986).
- [3] S. Chen and G. D. Doolen, Lattice Boltzmann method for fluid flows, *Ann. Rev. Fluid Mech.* **30**, 329 (1998).
- [4] D. H. Rothman and S. Zaleski, *Lattice-Gas Cellular Automata: Simple Models of Complex Hydrodynamics* (Cambridge University Press, Cambridge, 2004).
- [5] Z. Chai and B. Shi, A novel Lattice Boltzmann model for the Poisson equation, *Appl. Math. Modell.* **32**, 2050 (2008).
- [6] Z. Chai, B. Shi, and Z. Guo, A multiple-relaxation-time lattice Boltzmann model for general nonlinear anisotropic convection-diffusion equations, *J. Sci. Comput.* **69**, 355 (2016).
- [7] Z. Chai and T. S. Zhao, Lattice Boltzmann Model for the convection-diffusion equation, *Phys. Rev. E* **87**, 063309 (2013).
- [8] H. Wang, X. Yuan, H. Liang, Z. Chai, and B. Shi, A brief review of the phase-field-based lattice Boltzmann method for multiphase flows, *Capillarity* **2**, 33 (2019).
- [9] K. Connington and T. Lee, A review of spurious currents in the lattice Boltzmann method for multiphase flows, *J. Mech. Sci. Technol.* **26**, 3857 (2012).
- [10] T. Krüger, H. Kusumaatmaja, A. Kuzmin, O. Shardt, G. Silva, and E. M. Viggien, *The lattice Boltzmann method*, (Springer International Publishing, 2017).
- [11] Z. Guo and C. Shu, *Lattice Boltzmann method and its applications in engineering*, Vol. 3 (World Scientific, 2013).
- [12] H. Huang, L. Wang, and X. Lu, Evaluation of three lattice Boltzmann models for multiphase flows in porous media *Comput. Math. Appl.* **61**, 3606 (2011).
- [13] H. Liu, A. J. Valocchi, and Q. Kang, Three-dimensional lattice Boltzmann model for immiscible two-phase flow simulations, *Phys. Rev. E* **85**, 046309 (2012).
- [14] D. H. Kang and T. S. Yun, Minimized capillary end effect during CO₂ displacement in 2-D micromodel by manipulating capillary pressure at the outlet boundary in lattice Boltzmann method, *Water Resour. Res.* **54**, 895 (2018).
- [15] D. H. Kang and T. S. Yun, Transitional non-Darcy displacement of immiscible fluids due to inertial effect, *J. Hydrol.* **577**, 123934 (2019).
- [16] C. Pan, M. Hilpert, and C. T. Miller, Lattice-Boltzmann simulation of two-phase flow in porous media, *Water Resour. Res.* **40**, W01501 (2004).
- [17] H. Huang and X. Lu, Relative permeabilities and coupling effects in steady-state gas-liquid flow in porous media: A lattice Boltzmann study, *Phys. Fluids* **21**, 092104 (2009).
- [18] L. Hao and P. Cheng, Pore-scale simulations on relative permeabilities of porous media by lattice Boltzmann method, *Int. J. Heat Mass Transfer* **53**, 1908 (2010).
- [19] Y. Q. Zu and S. He, Phase-field-based lattice Boltzmann model for incompressible binary fluid systems with density and viscosity contrasts, *Phys. Rev. E* **87**, 043301 (2013).
- [20] H. Liang, B. C. Shi, Z. L. Guo, and Z. H. Chai, Phase-field-based multiple-relaxation-time Lattice Boltzmann Model for incompressible multiphase flows, *Phys. Rev. E* **89**, 053320 (2014).
- [21] F. Ren, B. Song, M. C. Sukop, and H. Hu, Improved lattice Boltzmann modeling of binary flow based on the conservative Allen-Cahn equation, *Phys. Rev. E* **94**, 023311 (2016).
- [22] M. Geier, A. Fakhari, and T. Lee, Conservative phase-field lattice Boltzmann model for interface tracking equation, *Phys. Rev. E* **91**, 063309 (2015).
- [23] A. G. Yiotis, J. Psihogios, M. E. Kainourgiakis, A. Papaioannou, and A. K. Stubos, A lattice Boltzmann study of viscous coupling effects in immiscible two-phase flow in porous media, *Colloids Surf. A* **300**, 35 (2007).
- [24] H. Liang, J. Xu, J. Chen, H. Wang, Z. Chai, and B. Shi, Phase-field-based lattice Boltzmann modeling of large-density-ratio two-phase flows, *Phys. Rev. E* **97**, 033309 (2018).
- [25] L. Zheng, T. Lee, Z. Guo, and D. Rumschitzki, Shrinkage of bubbles and drops in the lattice Boltzmann equation method for nonideal gases, *Phys. Rev. E* **89**, 033302 (2014).
- [26] M. Brassel and E. Bretin, A modified phase field approximation for mean curvature flow with conservation of the volume, *Math. Methods Appl. Sci.* **34**, 1157 (2011).
- [27] Y. Sun and C. Beckermann, Sharp interface tracking using the phase-field equation, *J. Comput. Phys.* **220**, 626 (2007).
- [28] P. H. Chiu and Y. T. Lin, A conservative phase field method for solving incompressible two-phase flows, *J. Comput. Phys.* **230**, 185 (2011).
- [29] Y. Hu, D. Li, L. Jin, X. Niu, and S. Shu, Hybrid Allen-Cahn-based lattice Boltzmann model for incompressible two-phase flows: The reduction of numerical dispersion, *Phys. Rev. E* **99**, 023302 (2019).
- [30] J. Rubinstein and P. Sternberg, Nonlocal reaction-diffusion equations and nucleation, *J. Inst. Math. Its Appl.* **48**, 249 (1992).
- [31] Z. Chai, D. Sun, H. Wang, and B. Shi, A comparative study of local and nonlocal Allen-Cahn equations with mass conservation, *Int. J. Heat Mass Transfer* **122**, 631 (2018).
- [32] W. J. Boettinger, J. A. Warren, C. Beckermann, and A. Karma, Phase-field simulation of solidification, *Annu. Rev. Mater. Sci.* **32**, 163 (2003).
- [33] T. Lee and L. Liu, Lattice Boltzmann simulations of micron-scale drop impact on dry surfaces, *J. Comput. Phys.* **229**, 8045 (2010).
- [34] D. d'Humières, in *Rarefied Gas Dynamics: Theory and Simulations*, Vol. 450 (1994).
- [35] P. Lallemand and L.-S. Luo, Theory of the lattice Boltzmann method: Dispersion, dissipation, isotropy, Galilean invariance, and stability, *Phys. Rev. E* **61**, 6546 (2000).
- [36] Z. Guo, C. Zheng, and B. Shi, Discrete lattice effects on the forcing term in the lattice Boltzmann method, *Phys. Rev. E* **65**, 046308 (2002).

- [37] A. Fakhari and T. Lee, Multiple-relaxation-time lattice Boltzmann method for immiscible fluids at high Reynolds numbers, *Phys. Rev. E* **87**, 023304 (2013).
- [38] J. U. Brackbill, D. B. Kothe, and C. Zemach, A continuum method for modeling surface tension, *J. Comput. Phys.* **100**, 335 (1992).
- [39] H. L. Wang, Z. H. Chai, B. C. Shi, and H. Liang, Comparative study of the lattice Boltzmann models for Allen-Cahn and Cahn-Hilliard equations, *Phys. Rev. E* **94**, 033304 (2016).
- [40] V. Joshi and R. K. Jaiman, A positivity preserving and conservative variational scheme for phase-field modeling of two-phase flows, *J. Comput. Phys.* **360**, 137 (2018).
- [41] S. A. Khan and A. Shah, Simulation of the two-dimensional Rayleigh-Taylor instability problem by using diffuse-interface model, *AIP Adv.* **9**, 1095 (2019).
- [42] N. Fleischmann, S. Adami, and N. A. Adams, Numerical symmetry-preserving techniques for low-dissipation shock-capturing schemes, *Comput. Fluids* **189**, 94 (2019).
- [43] Y. Ba, H. Liu, Q. Li, Q. Kang, and J. Sun, Multiple-relaxation-time color-gradient lattice Boltzmann model for simulating two-phase flows with high density ratio, *Phys. Rev. E* **94**, 023310 (2016).
- [44] D. Chiappini, G. Bella, S. Succi, F. Toschi, and S. Ubertini, Improved lattice Boltzmann without parasitic currents for Rayleigh-Taylor instability, *Commun. Comput. Phys.* **7**, 423 (2010).
- [45] T. Wei and D. Livescu, Late-time quadratic growth in single-mode Rayleigh-Taylor instability, *Phys. Rev. E* **86**, 046405 (2012).
- [46] J. Glimm, J. W. Grove, X. L. Li, W. Oh, and D. H. Sharp, A critical analysis of Rayleigh-Taylor growth rates, *J. Comput. Phys.* **169**, 652 (2001).
- [47] X. Zheng, N. Mahabadi, T. S. Yun, and J. Jang, Effect of capillary and viscous force on CO₂ saturation and invasion pattern in the microfluidic chip, *J. Geophys. Res.: Solid Earth* **122**, 1634 (2017).
- [48] Q. Zou and X. He, On pressure and velocity boundary conditions for the lattice Boltzmann BGK model, *Phys. Fluids* **9**, 1591 (1997).